

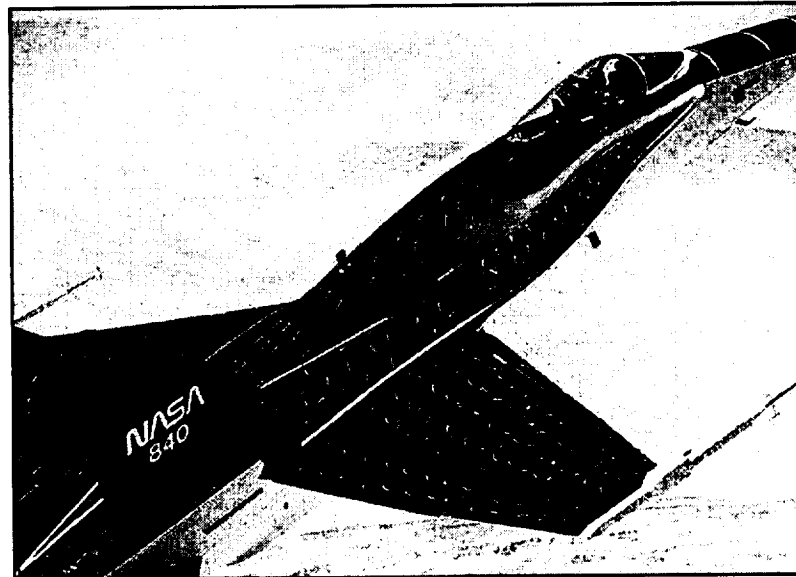
# High-Angle-of-Attack Technology Conference

## OVERVIEW OF HATP EXPERIMENTAL AERODYNAMICS DATA FOR THE BASELINE F/A-18 CONFIGURATION

Robert M. Hall, Daniel G. Murri, and Gary E. Erickson  
NASA Langley Research Center  
Hampton, Virginia

David F. Fisher and Daniel W. Banks  
NASA Dryden Flight Research Center  
Edwards, California

Wendy R. Lanser  
NASA Ames Research Center  
Moffett Field, California



September 17-19, 1996  
NASA Langley Research Center  
Hampton, Virginia



# OVERVIEW OF HATP EXPERIMENTAL AERODYNAMICS DATA FOR THE BASELINE F/A-18 CONFIGURATION

Robert M. Hall, Daniel G. Murri, and Gary E. Erickson  
NASA--Langley Research Center  
Hampton, VA

David F. Fisher and Daniel W. Banks  
NASA--Dryden Flight Research Center  
Edwards, CA

Wendy R. Lanser  
NASA--Ames Research Center  
Moffett Field, CA

## SUMMARY

Determining the baseline aerodynamics of the F/A-18 was one of the major objectives of the High-Angle-of-Attack Technology Program (HATP). This paper will review the key data bases that have contributed to our knowledge of the baseline aerodynamics and the improvements in test techniques that have resulted from the experimental program. Photographs are given highlighting the forebody and leading-edge-extension (LEX) vortices. Other data representing the impact of Mach and Reynolds numbers on the forebody and LEX vortices will also be detailed. The level of agreement between different tunnels and between tunnels and flight will be illustrated using pressures, forces, and moments measured on a 0.06-scale model tested in the Langley 7-by 10-Foot High Speed Tunnel, a 0.16-scale model in the Langley 30- by 60-Foot Tunnel, a full-scale vehicle in the Ames 80- by 120-Foot Wind Tunnel, and the flight F/A-18 High Alpha Research Vehicle (HARV). Next, creative use of wind tunnel resources that accelerated the validation of the computational fluid dynamics (CFD) codes will be described. Lastly, lessons learned, deliverables, and program conclusions are presented.

## INTRODUCTION

During the development of both the F-16 and F/A-18 programs, the ground testing community was tasked with predicting the flight characteristics of these configurations,

which had unprecedented abilities to go to high angles of attack and to develop significant vortical flows over their respective forebodies, strakes or leading-edge-extensions (LEX's), and wings. The interactions of these vortex systems have proved to be very nonlinear and very difficult to predict. It is the combination of the high angles of attack and the vortex system interactions that led to challenges for both of these development programs.

During each program, ground test predictions of either longitudinal or lateral/directional characteristics were found to be in error, or were called into question.<sup>1,2</sup> In order to bring some understanding to this situation, it was recognized that progress would have to be made in understanding the following for an advanced fighter: (1) the interactions among the different vortex systems, (2) the relationship between vortex bursting and vehicle stability, (3) the effects of Reynolds number on the vortical flows, and (4) the effects of Mach number on the vortical flows. It was also recognized that interpreting the apparent differences between tests in different tunnels would be necessary given the confusion that existed.

To address these concerns, the High-Angle-of-Attack Technology Program (HATP), chose the F/A-18 as a suitable configuration for exploring the above, and other, high-angle-of-attack issues. A critical factor in this decision process was the availability of the High Alpha Research Vehicle (HARV). Having flight data from the HARV, such as pressures, flow visualization, and parameter identification (PID), has been critical for validating both experimental and computational results. The in-depth instrumentation of the HARV for pressure measurements and for flow visualization has served as a model for later flight test efforts.

At the same time that the HARV was being developed and tested<sup>3-5</sup> during the HATP program, a vigorous experimental program was executed that involved many tests of the F/A-18 configuration in different tunnels. These tests used models ranging in size from a 0.03-scale model in the Basic Aerodynamics Research Tunnel at Langley<sup>6</sup> to a full-scale F/A-18 aircraft in the Ames 80- by 120-Foot Tunnel.<sup>7</sup> One of the successes of the overall HATP program was the good communication between the computational fluid dynamics (CFD) and the experimental communities. This led to a high degree of synergy between the CFD calculations and many of the experiments. While characterization of the baseline aerodynamics of the F/A-18 configuration was the thrust of Phase I of the HATP program,<sup>8</sup> additional work has continued since that time to specifically characterize Reynolds number and Mach number effects for the F/A-18, develop forebody gritting techniques for better simulation of “flight-like” boundary layers in conventional tunnels, and to explore other configuration issues.

In light of this conference serving as the “close out” of the HATP program, this paper will review the key experimental data sets, test techniques developed, and then examine a number of issues involving vortical flow physics. These issues involve vortical interactions, Reynolds number effects, and Mach number effects. Next, tunnel-to-tunnel

and limited tunnel-to-flight comparisons will be presented. Also, some unusual wind tunnel experiments will be highlighted that were specifically designed to assist the CFD community in code validation. The paper will then conclude with lessons learned, program deliverables, and program conclusions.

## SYMBOLS

The longitudinal data are referred to the stability-axis system and the lateral-directional data are referred to the body-axis system, see figure 1. The data are normalized by the usual quantities, such as planform area, span of the wing, and the wing mean aerodynamic chord. The moment reference center for the F/A-18 was located at 0.25 mean aerodynamic chord, which corresponds to full-scale fuselage station 458.6-in. All F/A-18 dimensions are given for the full-scale aircraft and can be calculated for each model size by appropriately scaling. The general dimensions of the F/A-18 are shown in figure 2.

b	reference wing span, 37.42 ft
$C_L$	lift coefficient, $\frac{\text{Lift}}{q_\infty S}$
$C_l$	body-axis rolling-moment coefficient, $\frac{\text{Rolling moment}}{q_\infty S b}$
$C_{l_\beta}$	derivative of $C_l$ with respect to $\beta$
$C_m$	pitching-moment coefficient referenced to 0.25 $\bar{c}$ , $\frac{\text{Pitching moment}}{q_\infty S \bar{c}}$
$C_{N,70-184}$	normal force coefficient for F/A-18 forebody as integrated from pressures from FS 70 to FS 184
$C_n$	body-axis yawing-moment coefficient, $\frac{\text{Yawing moment}}{q_\infty S b}$
$C_{n_\beta}$	derivative of $C_n$ with respect to $\beta$
$C_p$	static pressure coefficient, $\frac{p - p_\infty}{q_\infty}$
$C_p^*$	static pressure coefficient corresponding to sonic conditions
$\bar{c}$	wing mean aerodynamic chord, 11.52 ft
D	diameter of base of ogive or effective diameter of F/A-18 forebody at FS 184, 4.111 ft
FS, F. S.	fuselage station, inches full scale
M, $M_\infty$	free-stream Mach number
p	local static pressure, lb/ft <sup>2</sup>
$p_\infty$	free-stream static pressure, lb/ft <sup>2</sup>
$q_\infty$	free-stream dynamic pressure, lb/ft <sup>2</sup>

$R_{\bar{c}}$	Reynolds number based on $\bar{c}$
$S$	reference wing area, 400 ft <sup>2</sup>
$s$	local semispan distance from LEX-fuselage junction to LEX leading edge, ft
$y$	distance along LEX local semispan, ft
$\alpha$	angle of attack, deg
$\beta$	angle of sideslip, deg
$\beta_1, \beta_2$	angles of sideslip at which data were differenced to calculate $\beta$ -derivatives, deg
$\Delta C_{l_p}$	uncertainty in $C_{l_p}$
$\Delta C_{n_p}$	uncertainty in $C_{n_p}$
$\delta C_m$	incremental difference in pitching moment
$\delta_h$	deflection of horizontal tail, deg
$\theta$	forebody cross-section angular location (0° is bottom dead center, positive is clockwise as seen from pilot's view), deg

## KEY EXPERIMENTAL DATA SETS

During the characterization of the baseline configuration, a number of pivotal experiments were conducted that have significantly improved our understanding of the characteristics of the F/A-18. These experiments will be summarized and their contributions highlighted.

### Dryden Flight Tests of HARV Flight Vehicle

The flight tests were conducted at the NASA Dryden Flight Research Center using the F-18 HARV. The HARV, which is seen in figure 3, is a highly instrumented, preproduction single-place F/A-18 aircraft which was modified from the Navy preproduction spin test airplane. Its wing has both leading- and trailing-edge flaps that are scheduled with  $\alpha$  and  $M_\infty$ . At values of  $\alpha > 26^\circ$  and  $M_\infty < 0.76$ , the leading-edge-flap deflection angle goes to a maximum value of approximately  $34^\circ$  and the trailing-edge-flap deflection angle goes to  $0^\circ$ . The HARV was flown without stores and the wing tip missile rails have been modified to carry camera pods and wingtip airdata probes.

## DTRC 7- by 10-Foot Tests of 0.06-Scale Model

A series of David Taylor Research Center (DTRC) tests from 1987 to 1990 were conducted to document the F/A-18 forebody and LEX vortex flow characteristics at subsonic and transonic speeds with and without the LEX fences or flight test nose boom. These tests were a cooperative effort involving NASA, the U. S. Navy, and the McDonnell-Douglas Corporation. A photograph of the model in the tunnel is shown in figure 4.

The experiments were documented by Erickson in reference 9 and highlighted the maturing capability of laser vapor screen (LVS) technology. This tool, which will be discussed in the section on test techniques, was used very effectively by Erickson to clarify such issues as the role of vertical tails in lateral stability, the effect of  $M_\infty$  on the vortex structure over the LEX's, and the relative strengths of the forebody and LEX vortices. Erickson's work was an important contribution to the understanding of vortical flows.

## Ames 80- by 120-Foot Tests of Full-Scale Vehicle

As shown in figure 5, a single-seat full-scale F/A-18 aircraft, built by McDonnell Douglas Aircraft and the Northrop corporations, was tested in the NASA Ames Research Center 80- by 120-Foot Wind Tunnel. For the wind-tunnel tests, which occurred in 1991 and 1993, the aircraft had both engines removed, flow through inlets, the wing tip missile launch racks mounted, and the control surfaces configured for high- $\alpha$  flight. The data<sup>7</sup> utilized herein had the objective of obtaining baseline aerodynamics that could be used for comparisons with subscale wind tunnel and water tunnel tests, flight tests with the HARV, and CFD solutions. The data shown will be for the configuration without the LEX fences.

## Langley 7- by 10-Foot HST Test of 0.06-Scale Model

This 1992 experiment, which was a cooperative effort between NASA, the U. S. Navy, and McDonnell-Douglas Corporation, focused on the high- $\alpha$  performance of the F/A-18. An installation photograph showing the model in the 7- by 10-Foot High Speed Tunnel (HST) is shown in figure 6. The primary objective of this entry was to evaluate the high- $\alpha$  gritting patterns that were under development at Langley. Pressure data over the forebody and LEX's were obtained by mounting a Langley-manufactured forward

fuselage in the place of the usual forward fuselage for this model. Secondary objectives of the test were to reexamine the impact of the NACA nose boom on the lateral stability of the configuration with the leading-edge flaps deflected to 25° and 34°. Additional specialized data for computational fluid dynamics (CFD) code validation were obtained on the configuration without the horizontal and vertical tails.<sup>10</sup>

#### Langley LTPT Test of 0.06-Scale “Shroud” Model

Originally built to validate early CFD calculations over the F/A-18 forward fuselage in isolation, the configuration simulates the forebody and the LEX's of the F/A-18. This configuration consists of a Langley-manufactured, pressure-instrumented 0.06-scale forward fuselage attached to a sting by an adapter, called a “shroud,” which supports the forward fuselage in the tunnel and continues its cross section downstream, as shown in figure 7. The F/A-18 “Shroud” configuration was tested in the Langley Low-Turbulence Pressure Tunnel (LTPT) during 1994 to high- $\alpha$  at pressures up to 10 atmospheres and at Mach numbers up to 0.15 or 0.20, depending on maximum angle of attack. Because of the pressure capability, this test entry was able to determine the effects of Reynolds number on forebody pressure distributions for the same forebody used for much of the 0.06-scale F/A-18 testing.

#### Langley 30- by 60-Foot Tunnel Test of 0.16-Scale Model

This test also occurred in 1994 and utilized a high fidelity 0.16-scale model of the F/A-18. This model had an extensive set of pressures that more closely matched the flight set of pressures than did the 0.06-scale model. An installation photograph is shown in figure 8. The primary objectives of the test were documentation of the baseline configuration, determining the sensitivities of the configuration to forebodies with and without pressure orifices, and examining high- $\alpha$  gritting techniques.

### HIGHLIGHTS OF TEST TECHNIQUES DEVELOPED

One of the objectives of the HATP program was to foster the development of improved testing techniques that could lead to more effective experiments. To highlight the contributions of HATP in this area, three specific examples will be presented: advancements in the area of laser light sheet technology, in-flight flow visualization, and

advanced gritting patterns for high- $\alpha$  applications. The reader is referred to the cited references for more information.

### Laser Light Sheet Flow Visualization

This is a technology area that has been under development since 1951 (see reference 11). An evolution in quality of the light sheet and ease of its use has continued from that time. The HATP focus on vortical flows served as a catalyst and as an additional source of funding to advance the technology even further. Erickson in reference 9 was the first researcher to apply an advanced laser light sheet to investigate the vortical flow fields about the F/A-18. Examples of these laser vapor screen images will be given later in this report. Reference 9 contains several examples of how flow visualization can help explain the flow mechanisms behind the trends in the force and moment data. Erickson was also instrumental in introducing fiber-optics into the transonic wind tunnels at the Langley Research Center, which eliminated problems that were associated with mirror delivery systems in the usually high vibration environments of large, transonic wind tunnels. Many of the practical advances made by Erickson and others are documented in reference 12. The laser light sheet in combination with smoke was also used during the Ames 80- by 120-Foot Wind Tunnel test<sup>13</sup> and in the Langley 30- by 60-Foot Tunnel tests.<sup>14</sup>

### Flight Flow Visualization

Exciting advances in flow visualization for flight were pioneered during the HATP program. The HARV vehicle was modified<sup>3</sup> to include a smoke generation system, multiple cameras to record the flow fields, and a cockpit control system, as shown in figure 9. Using the smoke generation system, the team was able to get spectacular visualization of the LEX and forebody vortices. As shown in figure 10, this work was complemented by traditional tufting of the wing, body, and tails, which resulted in some dramatic images of the separation on the wing and vertical tails.

Other techniques were used to great advantage by the flight test personnel to characterize the flow past the vehicle surface. These techniques included an emitted fluid technique<sup>3</sup> which traced surface streamlines by using existing pressure orifices to emit a mixture of toluene-based red dye and propylene glycol monomethyl ether (PGME). The mixture then flowed back along the forebody or LEX and the PGME dried, leaving the dye as a permanent record which was photographed on the ground. A typical example of the quality of this work<sup>3</sup> is shown in figure 11. The importance of the flight flow visualization work can not be overemphasized because of the physical insights and

discoveries generated. For example, it was determined with the PGME that a laminar separation bubble on the flight vehicle forebody can extend as far as 40 in. aft of the nose before a fully turbulent separation pattern occurs for  $\alpha > 45^\circ$  (see reference 3).

### Forebody Gritting at High Values of Angle of Attack

High- $\alpha$  forebody gritting was developed to more accurately simulate flight-like boundary-layer separation at the low Reynolds numbers typically seen in conventional tunnels. Two gritting patterns were explored. First, a global, or distributed, gritting pattern was implemented to determine if there were any detectable differences with the forebody gritting. While it was realized that this distributed pattern might lead to excessive grit drag, initial analysis did not substantiate this and the pattern was used for several years during the early part of the program. The second, and more successful, pattern for transitioning the boundary layer at high- $\alpha$  has been to add twin, longitudinal strips at azimuthal angles between  $50^\circ$  and  $72^\circ$  from the windward plane of symmetry. The longitudinal strips are necessary because the flow about the forebody at high values of  $\alpha$  is predominantly in the cross-flow direction.

One such pattern is shown in figure 12, which is a photograph of the pattern on the 0.16-scale F/A-18 model in the Langley 30- by 60-Foot Tunnel. This pattern retains the conventional nose ring, which is effective for low-to-moderate values of  $\alpha$ , and adds the longitudinal twin strips, which are effective for high values of  $\alpha$ . The twin strips extend from the nose ring back to the fuselage station at which the LEX's begin. Similar gritting patterns were tested with the 0.06-scale F/A-18 model in the Langley 7- by 10-Foot HST, the 0.06-scale Shroud model in the Langley 7- by 10-Foot HST, and the 0.06-scale Shroud model in the Langley LTPT.

Most of the wind tunnel models as well as the flight vehicle had extensive pressure instrumentation at a number of forebody stations and LEX stations. Figure 13 highlights the pressure stations on the forebody and LEX's that will be referenced in the present paper. The forebody fuselage stations which manifest the largest differences in  $C_p$  between the conventionally gritted model data at low values of  $R\bar{c}$  and the HARV pressures at flight values of  $R\bar{c}$  are FS 142 and FS 184.

Dramatic improvements with the addition of the high- $\alpha$  gritting pattern are shown in figure 14 for the 1992 test of the 0.06-scale F/A-18 model in the Langley 7- by 10-Foot HST. The conventionally gritted model, labeled "Nose Ring" in figure 14, has a nose grit ring on the forebody while the advanced, high- $\alpha$  gritting pattern, labeled "#180 at  $72^\circ$ ," includes twin strips of #180 (0.0035-in. nominal size) grit at  $\pm 72^\circ$  from the windward plane of symmetry in addition to the conventional nose ring. The pressure distributions

about the respective forebody pressure rings are displayed as a function of  $\theta$ , the azimuthal angle about the forebody, for both the 0.06-scale model tested in the Langley 7- by 10-Foot HST and the HARV. Values of  $\theta = 0^\circ$  and  $360^\circ$  correspond to the windward plane of symmetry and a value of  $\theta = 180^\circ$  corresponds to the leeward plane of symmetry.

In figure 14, the peaks in  $C_p$  near  $\theta = 90^\circ$  and  $270^\circ$  at FS 85 and FS 107 result from the attached-flow maximum velocity regions as the flow reaches the maximum half-width of the fuselage, which is circular in cross section from the nose tip back through FS 107. High- $\alpha$  gritting has only a minor impact, for this example, at these forward two stations. For FS 142, the peaks in  $C_p$  near  $\theta = 75^\circ$  and  $285^\circ$  result from the attached-flow maximum velocity regions as the flow approaches the maximum half-width of the fuselage, which is no longer circular at this station. The conventionally gritted model data do not simulate the two suction peaks that are visible in the flight values of  $C_p$  near the leeward plane of symmetry,  $\theta = 160^\circ$  and  $200^\circ$ . These suction peaks are the result of the footprints of the flight forebody vortices. In contrast, the advanced gritting pattern does correctly simulate these vortex suction peaks of the flight pressures. At FS 184, the data using the advanced, high- $\alpha$  gritting pattern more closely simulate the flight recompression gradients on the leeward side near  $\theta = 120^\circ$  and  $240^\circ$  than do the data taken with the conventional nose ring alone. More details concerning the gritting technique are available in references 15 to 18.

The next high- $\alpha$  gritting example is for an early application to the F-16. This application was an attempt to simulate, at conventional wind tunnel Reynolds numbers, the pitching moment seen at high Reynolds number. Pitching moment data as a function of  $R\bar{c}$  from a Ames 12-Foot Tunnel test<sup>2</sup> are presented in figure 15. The added tick marks near the bottom of the plot correspond to the Reynolds numbers at which the early tests were conducted in the Langley 30- by 60-Foot Tunnel (LaRC in the plot), the General Dynamics Tunnel (GD), an earlier entry in the 12-Foot Tunnel (ARC), as well as the flight value of  $R\bar{c}$ . As can be seen in this figure, the various values of pitching moment predictions were dependent on  $R\bar{c}$ .

Consequently, the goal of the gritting test of the F-16 was to approximate the pitching moment at flight values of  $R\bar{c} \sim 8$  million while testing with a high- $\alpha$  gritting pattern at a value of  $R\bar{c} \sim 1.5$  million in the Langley 7- by 10-Foot HST with a 1/15-scale model. The test, as mentioned, was early in the gritting program and used a gritting pattern that incorporated a wedge shape of grit to transition the boundary-layer as shown in figure 16. As pointed out by Nakamura and Tomonari,<sup>19</sup> a pattern like this which places grit in the region of maximum attached-flow velocities can lead to excessive grit drag because of the larger losses in the boundary layer. Excessive grit drag can lead to

larger than usual normal force on the forebody and, consequently, excessive pitching moment.

With this concern in mind, the increments in the pitching moment coefficient due to the sector gritting pattern are compared to predictions based on an analysis by Hammett<sup>2</sup> in figure 17. Indeed, figure 17 shows that increments in pitching moment are overpredicted by roughly a factor of two by this gritting pattern. A better grit pattern like the twin-strip pattern would be expected to significantly reduce the overshoot in the gritting increment. In any case, the gritted data could have alerted the F-16 development program that significant Reynolds number effects might be in store for the flight vehicle.

## VORTICAL FLOW PHYSICS--INTERACTIONS

The next section summarizes some of the insights concerning vortical interactions that have been learned through the HATP program. The first examples will highlight how laser vapor screen images illustrate vortical flows for the 0.06-scale F/A-18 model in the DTRC tunnel.<sup>9</sup> The last example will demonstrate the ability of smoke visualization in flight to show the interaction between the forebody vortices and the LEX vortices.

### Burst Locations of LEX Vortices Near Vertical Tails

The power of the laser vapor screen technique to assist in data analysis is demonstrated in figure 18, which illustrates the effects of sideslip on the burst position of the LEX vortices for the tunnel conditions of  $M_\infty = 0.6$  and  $\alpha = 20^\circ$ . The top two images illustrate the state of the vortices when the light sheet is at FS 525. The image to the left is for  $\beta = 0^\circ$  while the image to the right is for  $\beta = 4^\circ$ . For the case where  $\beta = 0^\circ$ , the vortices are well organized and have not burst at this position upstream of the vertical tails. While hidden in this view by the vertical tails, the cores of these vortices are well defined and would appear, if visible, as dark voids in the center of the vapor highlighting the vortices. For the case of  $\beta = 4^\circ$ , the windward, or right, vortex has burst, as seen by the larger outer diameter of the vortex and by the "smearing" of the inner details of the vortex. The "smearing" results from the disruption of what had been a well defined core near the center of the unburst vortex.

The lower two photographs in figure 18 correspond to similar sideslip information taken further aft at FS 567, which is just downstream of the beginning of the vertical tail root chords. For this position at no sideslip, vortex burst has already taken place as evidenced by the lack of well-defined vortex cores. As shown by the lower photograph on

the right side for  $\beta = 4^\circ$ , the windward vortex remains burst and is even less well defined than for  $\beta = 0^\circ$ . However, the leeward vortex, which is burst at FS 567 for  $\beta = 0^\circ$ , has stabilized for  $\beta = 4^\circ$  and once again has an obvious vortex core visible. Thus, flow visualization demonstrates that in sideslip the windward vortex burst continues to progress forward, but the leeward vortex burst can actually move rearward. This information greatly increased the understanding of the relationship between vortex bursting and vehicle stability.

### Nose Boom Interactions with the Forebody Vortices

The presence of the NACA nose boom has also been found to be critical to the vortex interactions on the F/A-18.<sup>9,20,21</sup> Banks demonstrates in reference 20 that the nose boom impacts the oil flows over the forebody and canopy and also lessens the vortex footprint in the pressures measured over the forebody. An explanation of these effects is evident from figure 19, which shows laser light sheet information at FS 184 for the cases of nose boom off and nose boom on. For the case of boom off, there are two distinct vapor condensate regions highlighting the presence of the forebody vortices. For the case of boom on, the distinct forebody vortex regions have largely disappeared. That is, instead of two distinct forebody vortices, there is one nose boom wake region. The presence of the NACA nose boom appears to disrupt the formation or development of the forebody vortices. This disruption explains the lack of forebody vortex footprints in the oil flows of Banks<sup>20</sup> and the lack of vortex suction peaks in the forebody pressure distributions reported by Banks.<sup>20</sup> This disruption may also explain the degradation in the lateral stability of the F/A-18 with the NACA nose boom<sup>20</sup> since reference 21 reports that, in general, weakening the forebody vortices decreases the lateral stability of the F/A-18 for  $\alpha > 30^\circ$ .

### Forebody Vortices Interacting with LEX Vortices

A question that has been raised since the early 1980's concerns the interaction between the forebody vortices, LEX vortices, and wing flows. It was recognized by Chambers<sup>1</sup> that the forebody seemed to play a pivotal role in the determining the lateral stability of the F/A-18 vehicle. Furthermore, it was recognized that there must be some type of amplification process in the interactions between forebody and LEX vortex systems. That is, while the forebody vortices are relatively weak compared to the LEX vortices, it appears that modest changes to forebody vortices seem to amplify through the strength of the LEX vortices. A look at this interaction for the HARV flight vehicle is shown in figure 20, in which smoke has been used to trace both the forebody vortices and

the LEX vortices. As seen, the forebody vortices track over the canopy and aft along the fuselage before being pulled under the LEX vortex at a station just aft of the hingeline of the leading-edge flaps. This is just the type of interaction that Chambers and others had been hypothesizing to explain the behavior they had been observing.

## VORTICAL FLOW PHYSICS--REYNOLDS NUMBER EFFECTS

This section highlights some of the Reynolds number effects for the F/A-18 configuration that have been quantified during the HATP program. The first example of these effects will be a simple comparison between pressure data taken with the HARV at  $R_{\bar{c}} = 9.6$  million and the 0.06-scale model in the Langley 7- by 10-Foot HST at  $R_{\bar{c}} = 1.4$  million with a conventional nose ring of grit. This comparison for  $\alpha = 40^\circ$  is shown in figure 21 for four forebody pressure stations and is a subset of the data presented in figure 14. As seen before, the conventionally gritted wind tunnel data compare favorably to the flight data at FS 85 and FS 107. However, there are marked differences at FS 142 and FS 184. At FS 142, the forebody vortex footprints at  $\theta = 160^\circ$  and  $200^\circ$  for the flight data are totally absent in the wind tunnel data. Also, at FS 184, the azimuthal locations at which the flow begins to recompress on the leeward side,  $\theta = 135^\circ$  and  $225^\circ$ , are also different for the two values of  $R_{\bar{c}}$ . The lower Reynolds number data recompress at a more leeward azimuthal location than do the flight data. While agreement with the conventional gritting is satisfactory toward the front of the forebody, the agreement toward the aft end of the forebody is not satisfactory.

The next comparisons for Reynolds number effects are for the LEX pressure distributions. These data are shown in figure 22, which shows plots of upper surface pressure coefficient as a function of semi-span location along each LEX,  $y/s$ . A value of  $y/s = -1$  corresponds to the outboard edge of the left, or port, LEX. The values of  $y/s = 0$  correspond to the fuselage edge of either the port or starboard (right) LEX. Finally, the value of  $y/s = 1$  corresponds to the outboard edge of the starboard LEX. While there is much more scatter between the LEX data sets than there was for the forebody pressure data, the level of agreement between the two data sets is deemed acceptable based on several reasons. First, at  $\alpha = 40^\circ$ , LEX vortex burst location is observed to be unsteady both in the wind tunnel and flight and contributes to the uncertainty levels in  $C_p$ . Second, independent repeatability studies for both the 7- by 10-Foot data and the flight data suggest that the uncertainty in the respective values of  $C_p$  are on the order of  $\pm 0.1$ . A final reason for the differences is that the sense of the asymmetry, left to right, are reversed for the two sets of data. That is, at FS 253, the flight data have higher suction for the port vortex while the tunnel data have higher suction for starboard vortex. Ideally, neither set of data would be asymmetric left to right. That the differences between the tunnel data with its much smaller value of  $R_{\bar{c}}$  and the flight data with its much larger

value of  $R_{\bar{c}}$  are within the uncertainty levels of the two data sets suggests that there are no significant Reynolds number effects in the LEX pressures for  $R_{\bar{c}} \geq 1.4$  million.

To summarize, Reynolds number differences result in changes to the forebody pressure distributions at FS 142 and FS 184 but make no systematic change to the pressure distributions over the LEX's. Consequently, Reynolds number effects are considered to be an important factor on the forebody and not a significant factor on the LEX flows for  $R_{\bar{c}} \geq 1.4$  million.

## VORTICAL FLOW PHYSICS--MACH NUMBER EFFECTS

The next fundamental issue addressed was to resolve the magnitude of compressibility effects. To do this for the F/A-18 forebody, data will be utilized from two tests with the 0.06-scale Shroud model. The first test was conducted in the 7- by 10-Foot HST during 1990 and the second entry was the already mentioned entry in the LTPT during 1994. To address this question for the LEX pressures, data will be used from the 0.06-scale F/A-18 model tests in the DTRC 7- by 10-Foot Transonic Tunnel.

The two different experiments utilizing the Shroud model will, in combination with each other, provide information as to the approximate value of  $M_{\infty}$  at which compressibility effects begin on the forebody. During the first experiment in the 7- by 10-Foot HST, Reynolds number differences were created by varying  $M_{\infty}$  because the tunnel was a conventional, atmospheric facility. The second experiment utilized the LTPT pressure tunnel, which could vary Reynolds number independently of  $M_{\infty}$ . By integrating the pressures from the pressure rings on the forebody, a value of forebody normal force coefficient can be calculated. This coefficient used all five pressure rows on the forebody from FS 70 to FS 184 and is identified as  $C_{N,70-184}$ .

The data for the integrated normal force coefficient,  $C_{N,70-184}$ , from the two experiments are shown in figure 23, where the figure to the left shows  $C_{N,70-184}$  as a function of  $R_{\bar{c}}$  and the figure to the right shows  $C_{N,70-184}$  as a function of  $M_{\infty}$ . Although there is a small offset in the negative slopes of  $C_{N,70-184}$  in the left figure for  $0.4 < R_{\bar{c}} < 1.3$  million, both sets of data show the sharp drop in the value of  $C_{N,70-184}$  as the laminar flow over the majority of the forebody yields to the transitional flow pattern with its laminar separation bubble and reattachment.<sup>22</sup> Both data sets reveal a minimum in the value of  $C_{N,70-184}$  near a level of  $C_{N,70-184} = 1.0$  followed by an abrupt increase in the 7- by 10-Foot HST data at  $R_{\bar{c}} > 1.5$  million and a much more delayed, and gradual, increase in the LTPT data. Since, as indicated in the right hand figure, the LTPT data were taken at a constant, and low, value of  $M_{\infty}$ , one would expect the LTPT data to be without compressibility effects (see reference 23). Thus, the increase in the 7- by 10-Foot HST values of  $C_{N,70-184}$  for  $R_{\bar{c}} > 1.5$  million can be attributed to compressibility effects. The

value of  $M_\infty$  at which this increase becomes clear is highlighted with the solid symbol in both the figures and corresponds to a value of  $M_\infty = 0.4$ .

The next data set will be used to evaluate the magnitude of  $M_\infty$  effects over the LEX's for  $\alpha = 40^\circ$ . Figure 24 presents data taken during the DTRC entry with the 0.06-scale F/A-18 model and illustrates the differences in the LEX pressure distributions at the first LEX measurement station, FS 253. The distributions are shown for seven different values of  $M_\infty$  varying from 0.20 to 0.90. The distributions, which are all plotted to the same scale and without any offsets between curves, clearly reveal profound changes in the local distributions as a function of  $M_\infty$ . At the lower values of  $M_\infty$ , the distributions show distinct vortex suction peaks with  $C_p$  values as low as -3.3. As the value of  $M_\infty$  increases, the  $C_p$  distributions show less evidence of vortex peaks and gradually approach nearly constant levels of  $C_p = -1.2$  for  $M_\infty = 0.90$ . The extent of the compressibility effects was surprising, particularly at the low values of  $M_\infty$ , where changes in  $C_p$  were still occurring when  $M_\infty$  decreased from 0.3 to 0.2. While  $R\bar{c}$  varies from 1.0 million to 1.8 million for these different pressure distributions, this variation is not expected to be a factor because of the previously demonstrated insensitivity of LEX pressures to  $R\bar{c}$ .

Another example of how the laser vapor screen technique can assist in flow understanding is shown in figure 25. While laser vapor screen information was only available for  $M_\infty = 0.6$  and 0.8, it is clear that the structure that is present in the LEX vortices at  $M_\infty = 0.6$  becomes less defined at  $M_\infty = 0.8$ . This loss of structure seen in the laser vapor screen is consistent with the continuing reduction in the suction peaks in the pressure distributions when increasing  $M_\infty$  from 0.60 to 0.80. At the same time, an inboard and upward movement of the vortex can be noted for this same change in  $M_\infty$ . This movement away from the LEX surface would also be expected to reduce the vortex suction peaks.

## COMPARISON OF TUNNEL-TO-TUNNEL AND TUNNEL-TO-FLIGHT DATA

The tunnel-to-tunnel comparisons will examine both pressure distributions and forces and moments. The pressure data will be shown for pressure instrumented forebodies and LEX's on the 0.16-scale model in the Langley 30- by 60-Foot Tunnel, the 0.06-scale model in the Langley 7- by 10-Foot HST, the full-scale vehicle in the Ames 80- by 120-Foot Wind Tunnel, and the HARV flight vehicle. The force and moment information will come from the same three wind tunnel tests as well as lateral/directional stability information from the HARV.

## Pressure Data

The forebody pressure comparisons are shown in figure 26. The differences seen between the tunnel entries can, in general, be explained on the basis of Reynolds number effects. For example, at FS 85 and FS 107, the 0.16-scale model data, which has the lowest value of  $R_{\bar{c}} = 1.0$  million, show evidence of laminar separation bubbles near  $\theta = 135^\circ$  and  $225^\circ$ . It is difficult to know if any similar laminar separation bubbles are occurring in the data for the 0.06-scale model because of the sparseness of its pressure orifices. The only other differences of note for these first two fuselage stations are in the full-scale vehicle data from the 80- by 120-Foot Wind Tunnel test. These data have more negative levels of the attached-flow suction peaks near  $\theta = 90^\circ$  and  $270^\circ$  and more suction from the forebody vortices near  $\theta = 150^\circ$  and  $210^\circ$  at FS 107. Greater suction at FS 107 could be associated with boundary layer transition occurring further forward for this test, which would result in fully turbulent flow occurring further forward, which, in turn, results in the stronger forebody vortices. (See reference 18 for more discussion of forebody boundary-layer topologies and their impact on forebody vortex strength.) The 80- by 120-Foot Wind Tunnel data are corrected for blockage; however, there is no upwash correction applied to  $\alpha$ . This lack of correction in  $\alpha$  may also contribute to the more negative levels of attached flow suction at FS 85 and FS 107 and the increased vortex suction levels at FS 107.

The forebody pressure differences at FS 142 and FS 184 can, again, be explained on the basis of Reynolds number effects as well as physical differences between the full-scale vehicles and the subscale wind tunnel models. Both full-scale vehicles have their pressures influenced at FS 142 and FS 184 by a number of antenna covers, probes, and gun bay vents. Consequently, the pressures at these two aft forebody stations are quite choppy for both full-scale vehicles, which makes comparisons with the subscale models, which do not have these features, more difficult. Nevertheless, at FS 142 the primary differences are the presence of the strong vortex suction footprints at  $\theta = 160^\circ$  and  $200^\circ$  for both the full-scale vehicles and the complete absence of such footprints in both subscale model tests. At FS 184, the primary difference between the tests are in the azimuthal locations of the pressure recovery near  $\theta = 130^\circ$  and  $220^\circ$ . The higher Reynolds number data from both full-scale vehicles correspond to more windward positions for the pressure recovery.

The comparable LEX data are shown in figure 27 for all three LEX stations. If  $M_\infty$  effects were dominating the differences between the wind tunnels, then it would be expected that the data would be ordered so that those with the lower values of  $M_\infty$  would have the higher amount of suction under the LEX vortices for FS 253. This is generally true in figure 27 with the exception of the 7- by 10-Foot HST data with the 0.06-scale model, where  $M_\infty = 0.3$ . The 7- by 10-Foot HST data, shown by the squares, appear to

break with the  $M_\infty$  trend and this may be due to other differences, such as LEX geometry or uncertainty in the data. Other than the 7- by 10-Foot HST data set, all the other data do exhibit the  $M_\infty$  progression seen during the DTRC experiment. That is, at FS 253, the data from the 30- by 60-Foot Tunnel do have the highest suction peaks as would be anticipated for the lowest value of  $M_\infty = 0.08$ . The next highest level of suction is with the 80- by 120-Foot Tunnel data, where  $M_\infty = 0.15$ . The lowest value of suction at FS 253 corresponds to the flight data, where  $M_\infty = 0.25$ . The utility of knowing the progression of  $C_p$  with  $M_\infty$  is that one could identify that the LEX pressures from the 7- by 10-Foot HST test do not match the expected trends and then take other steps to resolve the anomaly, such as examining the geometry of those LEX's more closely or working to reduce the uncertainty in the pressure data.

### Force and Moment Data

The next comparisons presented will be for the forces and moments between the three wind tunnel experiments. The first comparison is shown in figure 28 and presents the lift coefficients measured during the experiments. The values of  $C_L$  appear to be similar for all of the tunnel experiments. In particular, the maximum values of  $C_L$  appear to be reasonably close for each of the three facilities. The values for the numerical maximum of  $C_L$  and the respective  $\alpha$  at which it occurs are 1.79 at  $\alpha = 38^\circ$  for the 30- by 60-Foot Tunnel, 1.81 at  $\alpha = 40^\circ$  for the 7- by 10-Foot HST, and 1.82 at  $\alpha = 40^\circ$  for the 80- by 120-Foot Wind Tunnel.

The second comparison is for pitching moment,  $C_m$ , and is shown in figure 29. For this coefficient, there are more distinct differences in the figure. First of all, the data from the 30- by 60-Foot Tunnel show more positive levels of pitching moment than do either of the other sets of wind tunnel data. However, separate work reported in reference 21 suggests that some of the difference between the 30- by 60-Foot Tunnel data and the 7- by 10-Foot HST tunnel data is due to the distortion of the aft end of the 0.06-scale model.

This distortion, shown in figure 30, includes a deformed region between the two engine exhausts and the deformed engine exhausts themselves, which are circular for the flight vehicle. The aft-end distortion is necessary to accommodate a centerline sting capable of transonic loads. Even when this aft-end flare of the 0.06-scale model was only crudely approximated during the test of the 0.16-scale model in the 30- by 60-Foot Tunnel, the increments in  $C_m$  between the distorted 0.16-scale model and the undistorted 0.16-scale model were about half the magnitude of the increment between the original 0.06-scale model data and the undistorted 0.16-scale model data. Consequently, the good agreement in figure 29 between the 7- by 10-Foot HST data and the Ames 80- by 120-

Foot Wind Tunnel data may be fortuitous. That is, if corrections for the effects of the aft-end distortion of the 0.06-scale model were applied to figure 29, then the 7- by 10-Foot HST  $C_m$  data would be increased and the disagreement with the 30- by 60-Foot Tunnel data would be cut in half. While one might question whether the mounting system in the 80- by 120-Foot Wind Tunnel may also be a factor, see figure 5, reference 24 reports that the effect of the mounting system would, if anything, increase the pitching moment. That is, any mounting correction to the 80- by 120-Foot Wind Tunnel data would be negative and increase the discrepancy with the 30- by 60-Foot Tunnel data. The reasons for the differences in the  $C_m$  data are not known at this time.

Since the original F/A-18 prototype experienced an unanticipated departure, there was high interest in determining if the ground test community could achieve some consistency in its predictions for lateral and directional stability. Consequently, the remainder of this section will focus on  $C_{l_p}$  and  $C_{n_p}$ . Data will be presented to give the level of reproducibility one might expect if one were to change the forebody of the models being tested. The next series of figures will compare the values of  $C_{l_p}$  and  $C_{n_p}$  obtained from the HARV flight vehicle, from the full-scale test at Ames, and from subscale tests at Langley.

The impact on  $C_{l_p}$  and  $C_{n_p}$  of changing forebodies on the 0.06-scale and 0.16-scale models is illustrated in figure 31. All of the data shown were taken with a horizontal tail setting of  $-12^\circ$ . Also,  $\beta_1$  and  $\beta_2$  given in the key of figure 31 are the values of  $\beta$  at which the data were differenced to calculate the derivative. Each of these two models was tested with more than one forebody. The 0.06-scale model was tested with both the Langley pressure-instrumented forward fuselage, labeled in the figure by forebody "Pressures," and the original non-instrumented forebody and LEX component, labeled in the figure by forebody "McAir." These 0.06-scale model data are shown in figure 31 by, respectively, the circles and the squares. As seen, just changing the forebody resulted in differences in  $C_{l_p}$  on the order of 0.0005 and slightly smaller differences in  $C_{n_p}$ . Comparable data for the 0.16-scale model are shown by the solid and dotted lines. The different 0.16-scale forebodies were built from the same mold but differed because one was pressure instrumented and one was not. The differences between the forebodies resulted in differences on the order of 0.001 in  $C_{l_p}$  and on the order of 0.0005 in  $C_{n_p}$  for  $30^\circ < \alpha < 50^\circ$ .

Thus, these stability data contain, in addition to traditional sources of tunnel uncertainty, uncertainty resulting from possible sensitivities to forebody geometry itself. For example, it can be important if the forebody is geometrically asymmetric left to right. Surface finish, or the presence of pressure orifices, can influence the data if they change the location of boundary-layer transition. On the basis of these two comparisons for the

0.06-scale and 0.16-scale models, it would appear that an effective uncertainty in  $\Delta C_{l_p}$  of  $\pm 0.001$  and in  $\Delta C_{n_p}$  of  $\pm 0.0005$  would be appropriate to represent these potential differences due forebody geometry sensitivities.

The next two figures summarize HARV data inferred from flight and are courtesy of Bowers from the Dryden Flight Research Center, see figure 32, and of Klein,<sup>25</sup> see figure 33. In figure 32(a), the  $C_{l_p}$  data of Bowers are plotted as a solid line as are his estimates for the uncertainty in the data, which are shown by the dotted lines. Up until  $\alpha = 40^\circ$ , the uncertainty in the data for  $C_{l_p}$  is on the order of  $\Delta C_{l_p} = \pm 0.001$ . At higher values of  $\alpha$ , the uncertainty is even larger. In figure 32(b), the  $C_{n_p}$  data of Bowers are given along with his estimates of uncertainty. The uncertainty estimates follow the same trend as was the case for  $C_{l_p}$ . The values of  $M_\infty$  and  $R\bar{c}$  are labeled as “n.a.” in figures 32 because the original values going into the differencing are not available to the present authors. These variables, however, are assumed to be on the order of  $M_\infty = 0.25$  and  $R\bar{c} \sim 8$  to 10 million. The values for  $\beta_1$  and  $\beta_2$  are also listed as “n.a.” because they are also not known to the authors; however, in a private communication with Mr. Bowers, the authors were informed that the data used for the differencing corresponded to  $|\beta| < 3^\circ$ .

The next figure, figure 33, includes the second set of HARV flight data from Klein.<sup>25</sup> As is shown in figure 33(a), there are differences in  $C_{l_p}$  between the two analyses that are outside the uncertainty levels associated with the Bowers analysis. These differences may result from the Bowers data being obtained later in the flight test program when thrust vectoring was installed with its attendant geometry differences, from different analysis methods, or from different  $\beta$ -ranges being used to calculate the derivatives. (Values of  $C_{l_p}$  can vary depending on the range of  $\beta$  used for the differencing process because of the nonlinearities that occur about  $\beta = 0^\circ$  for this configuration, see reference 18.) In any case, it is of interest to note that flight data, just like wind tunnel data, contain an element of uncertainty from flight test to flight test. With the exception of just one data point, the differences between the two flight data sets are within  $\Delta C_{l_p} = 0.015$  in the critical region of  $30^\circ < \alpha < 50^\circ$ .

The comparison between the Bowers data and the Klein data for  $C_{n_p}$  is shown in figure 33(b). Here the agreement is better. With the exception of one data point, the two sets of data are within  $\Delta C_{n_p} = \pm 0.001$  and, in general, the trends of the data are much more similar than was the case for  $C_{l_p}$ .

There are aspects of the flight data which make comparisons with the wind tunnel data more complicated. First, the flight data were taken with engine power generally set

to either military or afterburner. Varying engine power between these settings results in nozzle geometry changes at the fuselage end and leads to differences in inlet mass flow. The wind tunnel data shown for the 0.06-scale and 0.16-scale models did not include any effects of power or of thrust vectoring. Also, the Bowers flight data were obtained with thrust vectoring in use. Finally, the horizontal tail setting in flight varies to trim the vehicle while the tunnel data were generally obtained at a constant horizontal tail setting of  $-12^\circ$ .

The impact of these factors in flight testing on  $C_{l_p}$  --power on, thrust vectoring, and horizontal tail setting--can be estimated from existing data taken in the 30- by 60-Foot Tunnel with the 0.16-scale model. These estimates were summarized as follows by Murri for  $30^\circ < \alpha < 50^\circ$ :  $\Delta C_{l_p} = \pm 0.0005$  for power on,  $\Delta C_{l_p} = \pm 0.0002$  for thrust vectoring effects, and  $\Delta C_{l_p} = \pm 0.001$  (changes from more stable to less stable depending on horizontal tail setting and value of  $\alpha$ ) for horizontal tail variations. Doing a root-mean-square summation of these three sources of uncertainties when comparing the wind tunnel and the flight data leads to a value of  $\Delta C_{l_p} = \pm 0.0011$ . To get more of an overall sense of the uncertainty when comparing wind tunnel to flight data over the range of  $30^\circ < \alpha < 50^\circ$ , one can combine the above value for  $\Delta C_{l_p} = \pm 0.0011$  with the value of  $\Delta C_{l_p} = \pm 0.0010$  from the forebody sensitivities to get a cumulative value of  $\Delta C_{l_p} = \pm 0.0015$ .

The impact of these same factors in flight testing on  $C_{n_p}$  can also be estimated from the 30- by 60-Foot Tunnel data. These estimates were also summarized as follows by Murri for  $30^\circ < \alpha < 50^\circ$ :  $\Delta C_{n_p}$  due to power-on effects is as large as  $+0.0015$  for afterburner power and  $+0.001$  for military power,  $\Delta C_{n_p}$  is much smaller for thrust vectoring effects and is on the order of  $\pm 0.0005$ , and  $\Delta C_{n_p} = \pm 0.001$  (changes from more stable to less stable depending on horizontal tail setting and value of  $\alpha$ ) for horizontal tail variations. Notice that the impact of power effects for  $C_{n_p}$  is a bias change to increase  $C_{n_p}$  by an amount between  $+0.001$  and  $+0.0015$ . Doing a root-mean-square summation of the two remaining uncertainties from thrust vectoring and horizontal tail setting results in a value of  $\Delta C_{n_p}$  on the order  $= \pm 0.001$ . Thus to compare the wind tunnel data to flight data, it will be necessary to shift the tunnel data by an amount between  $+0.001$  and  $+0.0015$  and then to understand that other tunnel-to-flight differences result in an uncertainty level of  $\Delta C_{n_p} = \pm 0.001$ . The level of uncertainty will remain near  $\pm 0.001$  even when the forebody sensitivities are included because the forebody sensitivities were relatively smaller.

Figure 34 shows a comparison of data from the 80- by 120-Foot Wind Tunnel test with the two sets of flight data. The open squares highlight the data taken with the baseline radome installed on the full-scale vehicle and the solid squares represent the data taken with a modified radome fitted with the forebody strakes but with the strakes in the closed position. Once again, changing the radome and, in this case, adding slots and cutouts to accommodate the mechanical forebody strakes, resulted in differences in  $C_{l_p}$  on the order of 0.001, see figure 34(a), and differences in  $C_{n_p}$  of 0.002, see figure 34(b). However, given the large geometric changes to create the cutouts and slots in the strake radome, it was decided that the subscale model values of  $\Delta C_{l_p} = \pm 0.001$  and  $\Delta C_{n_p} = \pm 0.0005$  would be used to represent forebody sensitivities for the 80- by 120-Foot Wind Tunnel data. Combining the geometric sensitivities to the uncertainties associated with power-on effects, thrust vectoring effects, and horizontal tail setting effects, leads to the same cumulative values of uncertainty and bias as in the subscale data. These uncertainty bars for the 80- by 120-Foot Wind Tunnel data for  $C_{l_p}$  would always fall within the range of uncertainty of the Bowers flight data and would generally fall onto the curve fit for the Bowers flight data. The two most positive values of  $C_{l_p}$  in the open squares for the 80- by 120-Foot Wind Tunnel data are considered to be “out-of-trend” data and will not be repeated in further plots. The general agreement with  $C_{n_p}$  is much better, in general, although the 80- by 120-Foot Wind Tunnel data break positive near  $\alpha = 45^\circ$ , in contrast to the Bowers data, which appear to break positive near  $\alpha = 60^\circ$ .

The next comparison of the stability data is shown in figure 35 and shows the corresponding data for the subscale tests without advanced, high- $\alpha$  gritting. The 0.16-scale model data from the 30- by 60-Foot Tunnel test are shown by the solid diamonds and equilateral triangles while the 0.06-scale model data from the 7- by 10-Foot HST are shown by the solid right triangles. The two different 0.16-scale model data sets correspond to the pressure-instrumented and uninstrumented noses on the basic model. As shown in figure 35(a), the subscale model results appear to predict less negative values of  $C_{l_p}$  (less lateral stability) for  $30^\circ < \alpha < 45^\circ$  than do the flight data. The subscale  $C_{l_p}$  data are less negative than flight by as much as 0.001 for the Klein analysis and as much as 0.002 for the Bowers analysis. The difference with the Klein data is within the comparison uncertainty level of  $\Delta C_{l_p} = \pm 0.0015$ , but the difference from the Bowers data is outside that uncertainty estimate.

The corresponding information for  $C_{n_p}$  are shown in figure 35(b). While there are still some scatter in the data for the low values of  $\alpha < 30^\circ$ , there is, at first glance, excellent agreement between the subscale data and both sets of flight data between  $30^\circ < \alpha < 40^\circ$ . What makes this apparent agreement illusory is that the wind tunnel data require a correction of between +0.001 to +0.0015 to account for power-on effects.

Between  $40^\circ < \alpha < 50^\circ$ , the agreement of the data degrades as the data sets begin to differ by as much as 0.002, which is on the order of Bowers uncertainty in  $C_{n_p}$  in this range of  $\alpha$ .

The impact that gritting has on the subscale to flight comparisons is presented in reference 18. As is discussed in that report, the impact of gritting on the  $C_{l_p}$  data is inconclusive because of the large differences in the flight data. However, the better agreement in  $C_{n_p}$  of the flight data provides a better “yardstick” and led to the conclusion in reference 18 that the gritted subscale data do a better job of simulating the high Reynolds number data than do the conventionally gritted data.

## EXPERIMENTS DESIGNED TO PROVIDE CFD WITH STRATEGIC DATA

Creative examples of using the wind tunnel to help validate CFD code work are presented next. This work highlights the successful communication between the experimentalists and the CFD specialists during the HATP program. The examples include a low Reynolds number test, a specially designed fixture for an existing model component, and a very unusual vehicle configuration.

The first example came early in the CFD program when the first CFD calculations at Langley were completed over a configuration which represented only the F/A-18 forebody and LEX's, see reference 26. At the time, both laminar and turbulent calculations were performed. Because there were many initial questions concerning the accuracy of the turbulence modeling, it was realized that if the experimental community could provide CFD with test data for values of  $R\bar{c}$  low enough to ensure laminar flow down the forebody, then the tunnel data could validate the laminar calculations. This challenge was accepted by the experimental community and resulted in oil flow streamline visualizations being obtained in the Langley BART tunnel<sup>6</sup> that compared quite favorably with the Navier-Stokes predictions of the laminar flow as shown in figure 36. (Note that in this and later figures free-stream Mach number is denoted by the letter M.) By acquiring experimental data in the laminar regime, key validation information was provided to the CFD community to confirm that their codes were indeed simulating the correct physics for laminar flow.

The second example also involved the early calculations on the isolated forebody/LEX configuration. Samples of these calculations are shown in figure 37 and illustrate the early concern. In order to conserve computer resources during the late 1980's, the CFD model did not represent the F/A-18 wings, aft fuselage, or empennage. Instead, the CFD model aft of the LEX's was just a rearward extension of the cross section at the aft end of the LEX's. While the results of the computation on the forebody

agreed well with flight and experimental data for the full configuration, the predicted pressures on the LEX's did not. Whether these differences in the LEX pressures were due to the presence of the wings and empennage on the full configuration or whether the differences were due, at least in part, to shortcomings of the flow solver needed to be resolved.

This concern was addressed by building an experimental model designed to look just like the CFD configuration. This experimental model combined the existing, pressure-instrumented Langley forward fuselage component for the F/A-18, which consisted of the forebody and LEX's, with a new aft component duplicating the cross section used in the calculations, as shown in figure 38. This new component was a fairing, or "shroud." When the pressure data over the LEX's for the shroud configuration were compared to the CFD pressures, it was clear that the differences noted between the full configuration pressures and the CFD calculations were, in fact, due to the more simplified geometry involved with the CFD calculation and not due to shortcomings of the CFD flow solver.

The final example also involved a case of the experiment assisting the CFD because of a less than complete representation of the geometry during the CFD calculation. As shown in figure 39, a detailed CFD computation was performed at Langley for a representation of the F/A-18 that did not include the presence of the twin tails, horizontal tails, or flow-through engine inlets. During the same time period, the 0.06-scale model of the F/A-18 configuration was being tested in the Langley 7- by 10-Foot HST. The experimental program was augmented by adding a few runs for which the configuration was modified by removing the vertical and horizontal tails and fairing over the inlets. This configuration is shown in the photograph of figure 40. With the modified model data available, the CFD community was able to demonstrate excellent agreement between predicted values of forces and moments and the actual values measured during the experiment with the modified configuration (see reference 10).

## SUMMARY REMARKS

### Lessons Learned

While the aerodynamics community had suspected that vortical interactions were complex and very nonlinear, this was not fully documented and quantified until the HATP program. For example, the forebody vortices over the F/A-18 are relatively weak compared to the LEX vortices. However, the impact of Reynolds number or of advanced forebody gritting can change the strength of the forebody vortices and impact the value of rolling moment for the entire configuration.<sup>18</sup> With the application of sophisticated off-

body flow visualization techniques, both in the wind tunnel and flight, the location of vortex bursting for the LEX vortices were documented. Also, it was established that relatively minor changes to the configuration can dramatically impact configuration stability and control. For example, small differences in forebody shapes, both in wind tunnel models and in production F/A-18's, have significant impacts on the levels of lateral stability. In addition, the presence of the NACA nose boom on the front of the aircraft was seen to have an extremely large impact on lateral stability.<sup>20</sup>

Reynolds number effects on smooth-sided forebodies were also identified as an important factor for aircraft with this type of forebody. Reynolds number effects were shown to be responsible for some of the systematic differences between the flight and the wind tunnel forebody pressure data. Another interesting discovery during the flight program was that the full-scale vehicle had evidence of laminar separation as far aft as 40 in. from the tip of the forebody at angles of attack greater than  $45^\circ$ . This realization is important because it demonstrates that forebody gritting in the wind tunnel can trigger fully turbulent flow too far forward on the forebody and that the CFD community may eventually have to model the laminar separation and reattachment for forebody flows if solutions are going to simulate all of the flow physics over the forebody. Reynolds number effects on the F/A-18 LEX's were shown not to be significant.

The impact of Mach number on the forebody and LEX flow fields has also been documented. For example, the Mach effects on the forebody pressure distributions begin for  $M_\infty > 0.30$  at  $\alpha = 40^\circ$  and result in modest differences in the integrated normal force. In contrast, the Mach effects on the LEX's begin at values of  $M_\infty$  below 0.2 and result in very strong loading differences on the LEX upper surfaces.

Finally, wind tunnel experimental programs can be creatively used to support CFD validation by modifying models to match the geometry fidelity compromises that are sometimes made by the CFD community to get the solutions in a timely way and with reasonable computer resources. The close cooperation between the experimental and CFD communities was a factor in the rapid progress made by the CFD community in modeling the highly separated flows about the F/A-18 during the life of the HATP program.

## Deliverables

A systematic flight and wind tunnel data base, which is truly unique in scope, has been established which includes force and moments, surface pressures, and limited on- and off-body flow visualization information. The data base addresses the performance and stability and control of the basic F/A-18 vehicle, fundamental vortical flow

interactions, Reynolds number effects, Mach number effects, tunnel-to-tunnel comparisons, and tunnel-to-flight comparisons.

Other deliverables include the present day availability of sophisticated flow visualization capabilities for flight. These techniques were dramatically improved during the life of the HATP program in the areas of surface flow visualization capability and of high quality off-surface flow visualization through the means of injecting smoke into the cores of both the forebody and LEX vortices.<sup>3</sup> Truly, the state of the art for in-flight visualization was redefined during the HATP program.

Laser light sheet capability for wind tunnels also progressed during the life of the HATP program. Modern laser light sheets routinely use fiber-optic means of transmitting the laser light into the facility. None of this was standard during the mid-1980's when running a laser light sheet in a transonic tunnel required hours of alignment each day by laser specialists. Today, it can be a turnkey operation as a result of many of the innovations prompted by the HATP program.<sup>12</sup>

Advanced forebody gritting techniques for high-angle-of-attack conditions were developed and demonstrated during the HATP program. It was found that the grit pattern is important and that a twin-strip pattern with the strips oriented longitudinally downstream of a conventional nose ring is optimal. The presence of the high- $\alpha$  gritting greatly improves the forebody pressure simulation in the wind tunnel for the aft portion of the forebody. The high- $\alpha$  gritting is considered a good technique to better simulate flight-like pressures and forces and moments in the wind tunnel but is not considered an exact solution.<sup>18</sup> The high- $\alpha$  gritting also reduced differences in tunnel-to-tunnel data comparisons for subscale model tests.<sup>18</sup>

A better understanding of both Reynolds number and Mach number effects can now be employed to explain many of the tunnel-to-tunnel data differences that exist when a number of models and facilities are involved in a test program. Most of the differences found in testing the 0.06-scale model in the Langley 7- by 10-Foot HST, the 0.16-scale model in the Langley 30- by 60-Foot Tunnel, and the full-scale vehicle in the Ames 80- by 120-Foot Wind Tunnel can be understood on this basis.

The credibility of wind tunnel testing has been confirmed for the high- $\alpha$  regime. After the initial departure of the F/A-18 prototype and the apparently conflicting experimental data<sup>1</sup> obtained during the original F/A-18 development program, it has now been shown that similar results for lateral and directional stability are obtained for similar geometric configurations. Tunnel-to-tunnel stability differences that do arise can be explained, by and large, by the uncertainty levels due to forebody geometric sensitivities. Differences between tunnel and flight data fall within the uncertainty levels associated

with both the forebody sensitivities and the other uncertainty sources arising from power-on effects, thrust vectoring, and horizontal tail deflections.

### Programmatic Conclusions

In terms of conclusions for the HATP program itself, it was found that having a highly instrumented flight vehicle was critical to establish the credibility of the ground test information and the CFD results. Furthermore, coordinating the instrumentation packages of both the flight vehicle and the wind tunnel models was an important step in expediting critical comparisons of the various data sets. Also, being able to compare the on- and off-body flow visualization data between flight, wind tunnel, and CFD has proved invaluable. Finally, the high value of the data comparisons was the result of one of the most successful aspects of the program--close communications and working relationships between the flight, ground test, and CFD technical communities.

### REFERENCES

1. Chambers, J. R.: High-Angle-of-Attack Aerodynamics: Lessons Learned. AIAA Paper No. 86-1774-CP, June 1986.
2. Hammett, L. N., Jr.: An Investigation of the F-16 High-Angle-of-Attack Pitching-Moment Discrepancy. Technical Report AFWAL-TR-81-3107.
3. Fisher, D. F.; Del Frate, J. H.; and Richwine, D. M.: In-Flight Flow Visualization Characteristics of the NASA F-18 High Alpha Research Vehicle at High Angles of Attack. NASA TM 4193, May 1990.
4. Fisher, D. F.; Banks, D. W.; and Richwine, D. M.: F-18 High Alpha Research Vehicle Surface Pressures: Initial In-Flight Results and Correlation With Flow Visualization and Wind-Tunnel Data. NASA TM 101724, August 1990.
5. Fisher, D. F.; and Cobleigh, B. R.: Controlling Forebody Asymmetries in Flight--Experience With Boundary Layer Transition Strips. NASA TM 4595, July 1994.
6. Sellers, W. L.; Meyers, J. F.; and Hepner, T. E.: LDV Surveys Over a Fighter Model at Moderate to High Angles of Attack. SAE Technical Paper 881448, Aerospace Technology Conference and Exposition, Anaheim, California, Oct 3-6, 1988.
7. Lanser, W. R.; Meyn, L. A.; Botha, G. A.; Ross, J. C.; James, K. D.; Hall, R. M.; and Murri, D. G.: Overview of Full-Scale F/A-18 Tests in the 80- by 120-Foot Wind Tunnel with Small-Scale Comparisons. High-Angle-of-Attack Technology Conference, NASA Langley Research Center, Hampton, Virginia, September 17-19, 1996.
8. Gilbert, W. P.; and Gatlin, D. H.: Review of the NASA High-Alpha Technology Program. NASA CP-3149, Volume 1, Part 1, 1992, pp. 23-59.

9. Erickson, Gary E.: Wind Tunnel Investigation of Vortex Flows on F/A-18 Configuration at Subsonic Through Transonic Speeds. NASA TP 3111, December 1991.
10. Ghaffari, Farhad: Navier-Stokes, Flight, and Wind Tunnel Flow Analysis for the F/A-18 Aircraft. NASA TP 3478, December 1994.
11. Allen, H. Julian; and Perkins, Edward W.: A Study of Effects of Viscosity on Flow Over Slender Inclined Bodies of Revolution. NACA Rep. 1048, 1951. (Supersedes NACA TN 2044.)
12. Erickson, G. E.; and Inenaga, A. S.: Fiber-Optic-Based Laser Vapor Screen Flow Visualization System for Aerodynamic Research in Larger Scale Subsonic and Transonic Wing Tunnels. NASA TM 4514, January 1994.
13. Lanser, W. R.; Botha, G. J.; and , J. P.: Flow Visualization Applied to a Full-Scale F/A-18 Aircraft in a Wind Tunnel Test. Flow Visualization VII Proceedings of the Seventh International Symposium on Flow Visualization, ed. J. Crowder, Begell House, New York, 1995, pp. 922 - 928.
14. Murri, D. G.; Shah, G. H.; DiCarlo, D. J.; and Trilling, T. W.: Actuated Forebody Strake Controls for the F-18 High Alpha Research Vehicle. AIAA Journal of Aircraft, Vol. 32, No. 3, May/June 1995, pp. 555-562.
15. Hall, R. M.; Erickson, G. E.; Banks, D. W.; and Fisher, D. F.: Advances in High-Alpha Experimental Aerodynamics: Ground Test and Flight. NASA CP-3149, Volume 1, Part 1, 1992, pp. 69-115.
16. Hall, R. M.; and Banks, D. W.: Progress in Developing Gritting Techniques for High Angle of Attack Flows. AIAA Paper No. 94-0169, January 1994.
17. Hall, R. M.; Banks, D. W.; Fisher, D. F.; Ghaffari, F.; Murri, D. G.; Ross, J. C.; Lanser, W. R.; A Status Report on High Alpha Technology Program (HATP) Ground Test to Flight Comparisons. Fourth NASA High Alpha Conference, Dryden Flight Research Center, July 12-14, 1994.
18. Hall, R. M.; Sewall, W. G.; Murri, D. G.; Allison, D. O.; and Banks, D. W.: Simulating High Reynolds Number Flows at High- $\alpha$  With Advanced Forebody Gritting Patterns. High-Angle-of-Attack Technology Conference, NASA Langley Research Center, Hampton, Virginia, September 17-19, 1996.
19. Nakamura, Y., and Tomonari, Y., The Effects of Surface Roughness on the Flow Past Circular Cylinders at High Reynolds Numbers. J. Fluid Mech, Vol. 123, 1982, pp. 363 to 378.
20. Banks, D. W.; Hall, R. M.; Erickson, G. E.; and Fisher, D. F.: Forebody Flow Field Effects on the High Angle-of-Attack Lateral-Directional Aerodynamics of the F/A-18. AIAA Paper No. 94-0170, January 1994.
21. Banks, D. W.; Fisher, D. F.; Hall, R. M.; Erickson, G. E.; Murri, D. G.; Grafton, S. B.; and Sewall, W. G.: The F/A-18 High-Angle-of-Attack Ground-to-Flight Correlation: Lessons Learned. High-Angle-of-Attack Technology Conference, NASA Langley Research Center, Hampton, Virginia, September 17-19, 1996.
22. Lamont, P. J.: Pressures Around an Inclined Ogive Cylinder with Laminar, Transitional, or Turbulent Separation. AIAA Journal, Vol. 20, No. 11, November 1982, pp. 1492-1499.

23. Polhamus, E. C: A Review of Some Reynolds Number Effects Related to Bodies at High Angles of Attack. NASA CR 3809, August 1984.
24. Sommers, J. D., "An Experimental Investigation of Support Strut Interference on a Three-Percent Fighter Model at High Angles of Attack", Masters Thesis at Naval Postgraduate School. Sept. 1989.
25. Klein, V.; Ratvasky, T. P.; and Cobleigh, B. R.: Aerodynamic Parameters of High-Angle-of-Attack Research Vehicle (HARV) Estimated from Flight Data. NASA TM 102692, August 1990.
26. Ghaffari, F.; Luckring, J. M.; Thomas, J. L.; and Bates, B. L.: Navier-Stokes Solutions About the F/A-18 Forebody Leading-Edge Extension Configuration. *Journal of Aircraft*, Vol 27, Number 9, Sept. 1990, pp. 737-748.

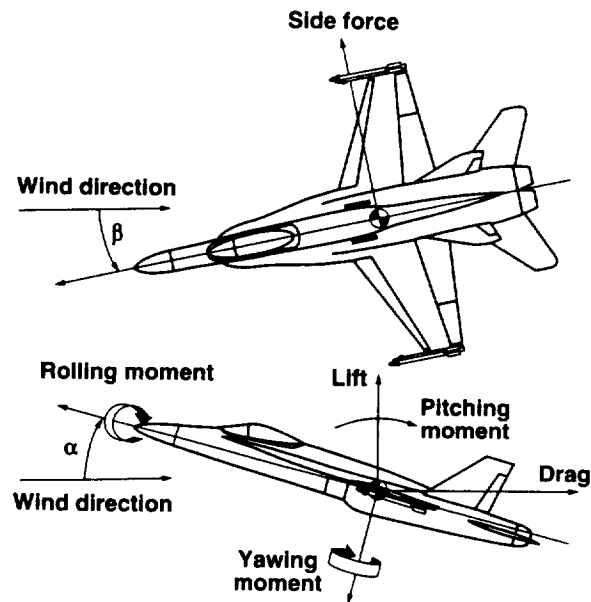


Figure 1.--Positive directions of forces, moments, velocities, and angles.

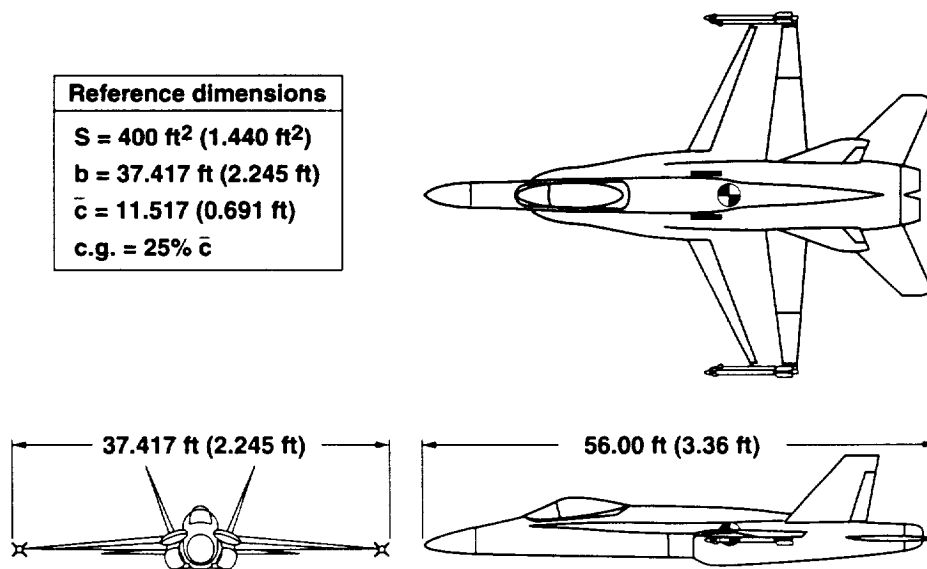


Figure 2.--F/A-18 geometry details. Dimensions are in feet full scale (0.06-scale).

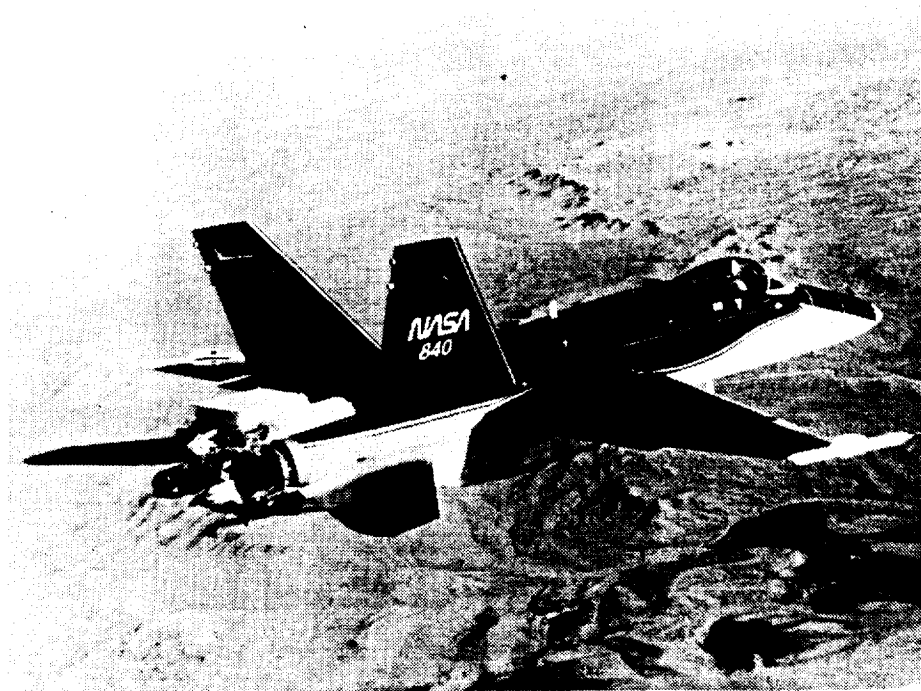


Figure 3.--NASA F-18 HARV in flight.



Figure 4.--0.06-scale F/A-18 model in the David Taylor Research Center 7- by 10-Foot Transonic Tunnel.

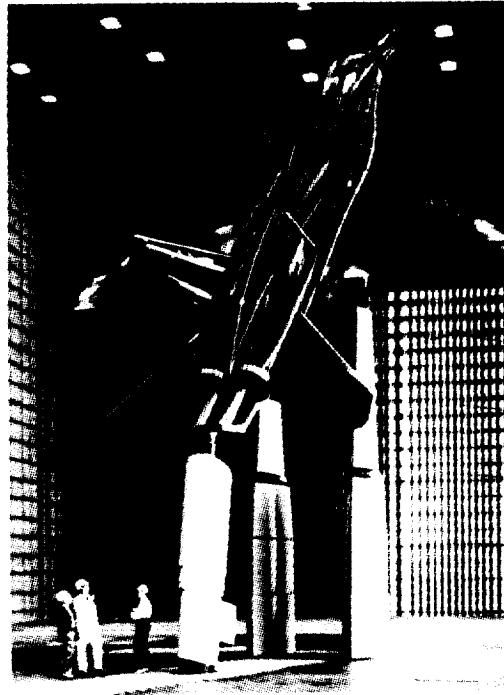


Figure 5.--Full-scale vehicle in the Ames 80- by 120-Foot Tunnel.

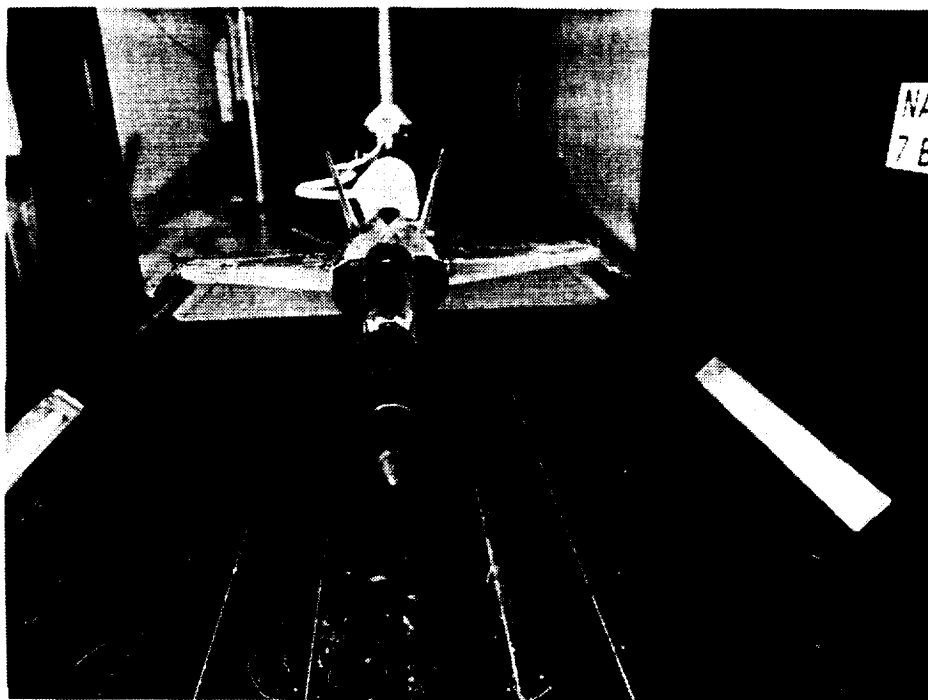


Figure 6.--0.06-scale model of F/A-18 in Langley 7- by 10-Foot High Speed Tunnel.

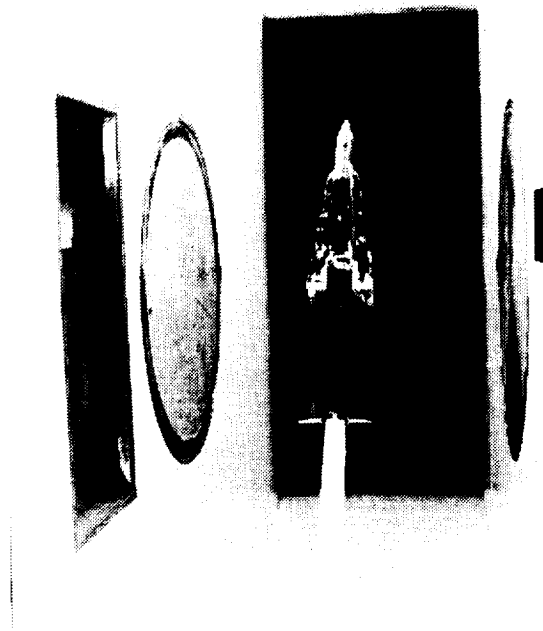


Figure 7.--0.06-scale Shroud model installed in the Langley Low Turbulence Pressure Tunnel (LTPT).

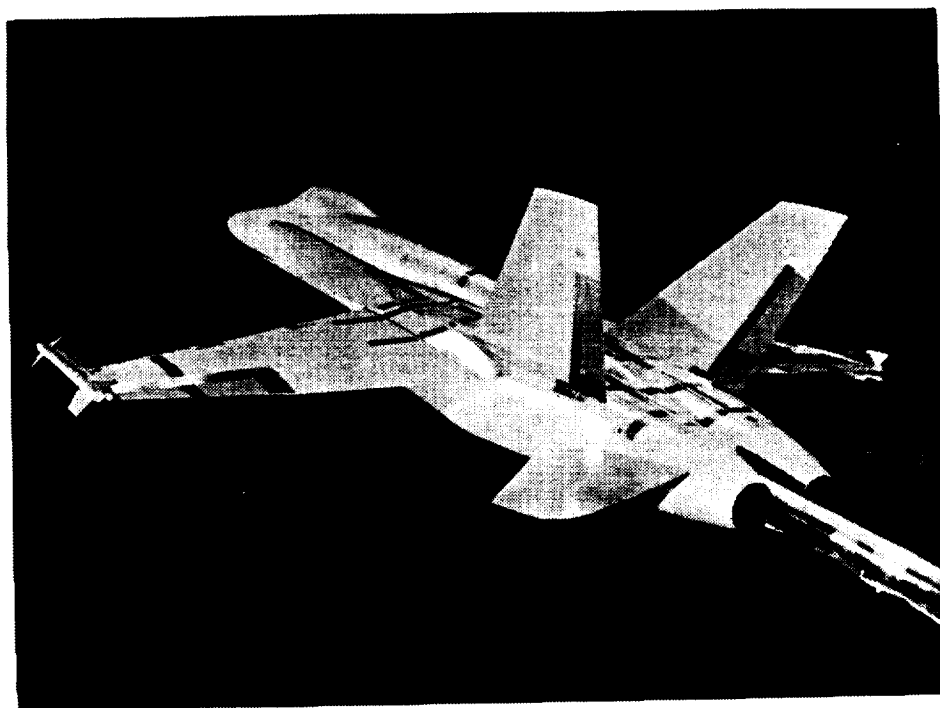


Figure 8.--0.16-scale F/A-18 model installed in the Langley 30- by 60-Foot Tunnel.

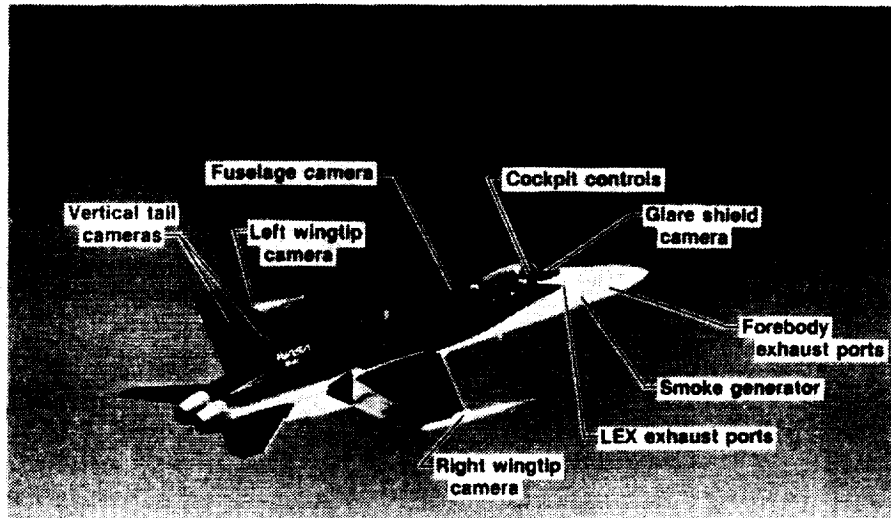


Figure 9.--Camera locations on NASA HARV Aircraft.

### Surface Flow Visualization

Tuft Technique on Wing and LEX,  $\alpha \sim 25^\circ$

NASA  
AD90-340

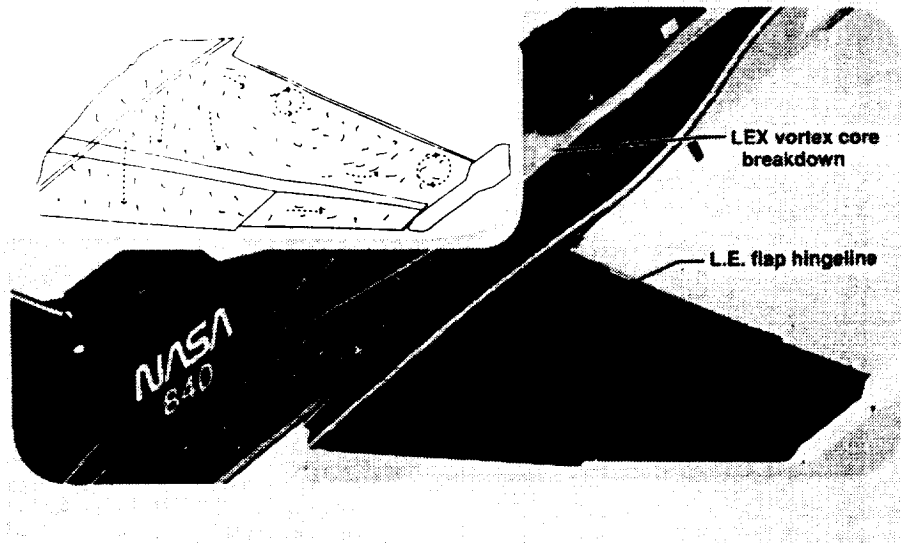


Figure 10.--Surface flow visualization on the HARV vehicle.

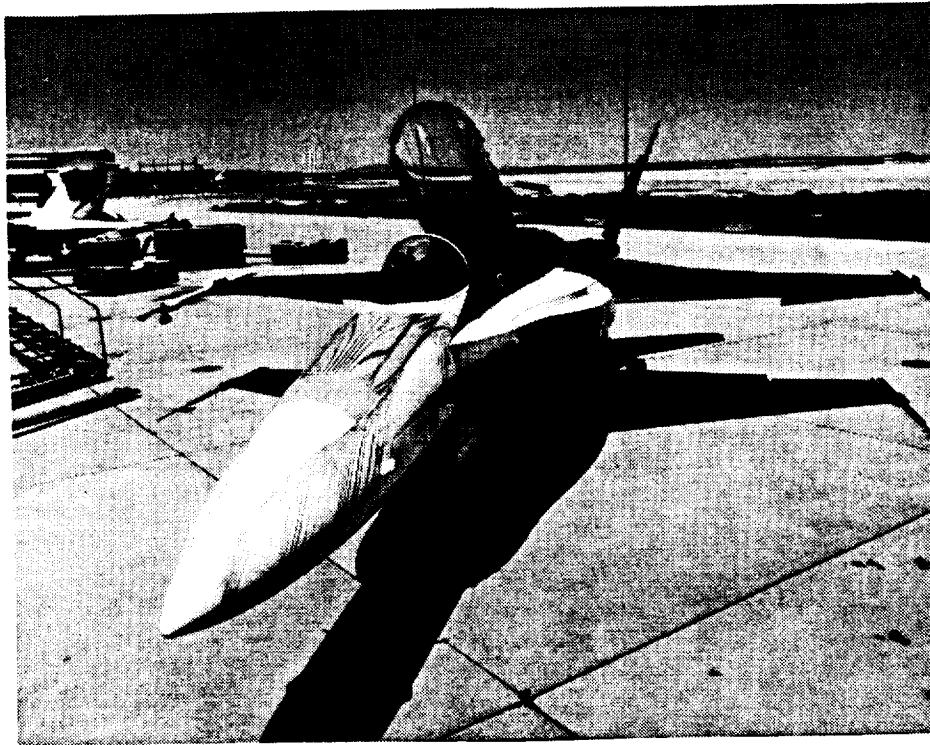


Figure 11.--Forebody surface flow images using PGME process on HARV vehicle.

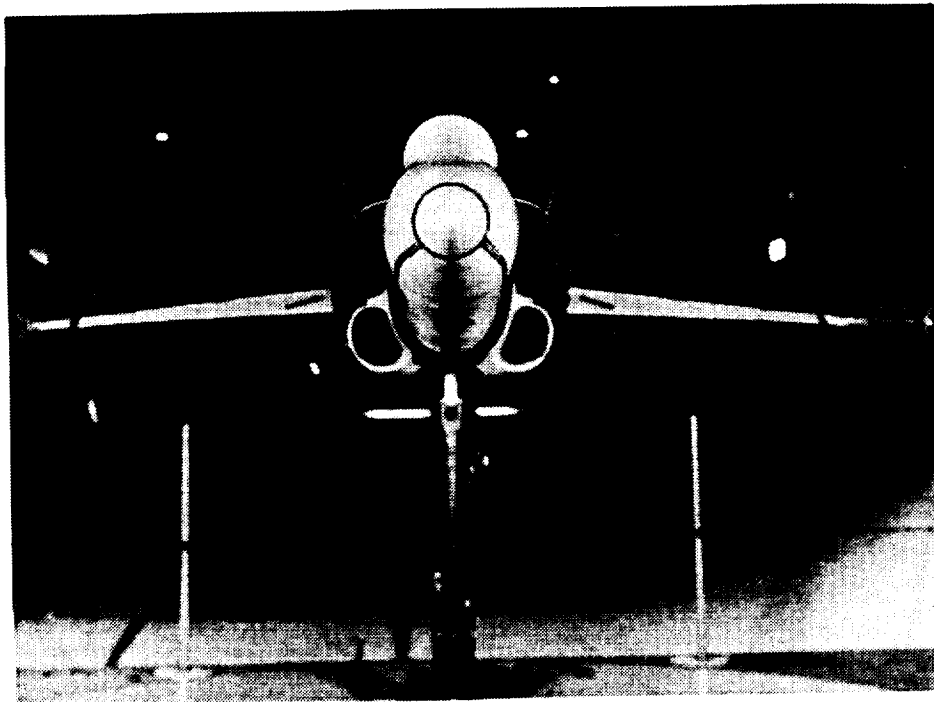


Figure 12.--High- $\alpha$  gritting pattern used during test of 0.16-scale F/A-18 model in 30- by 60-Foot Tunnel. Note nose ring and longitudinal twin strips on forebody.

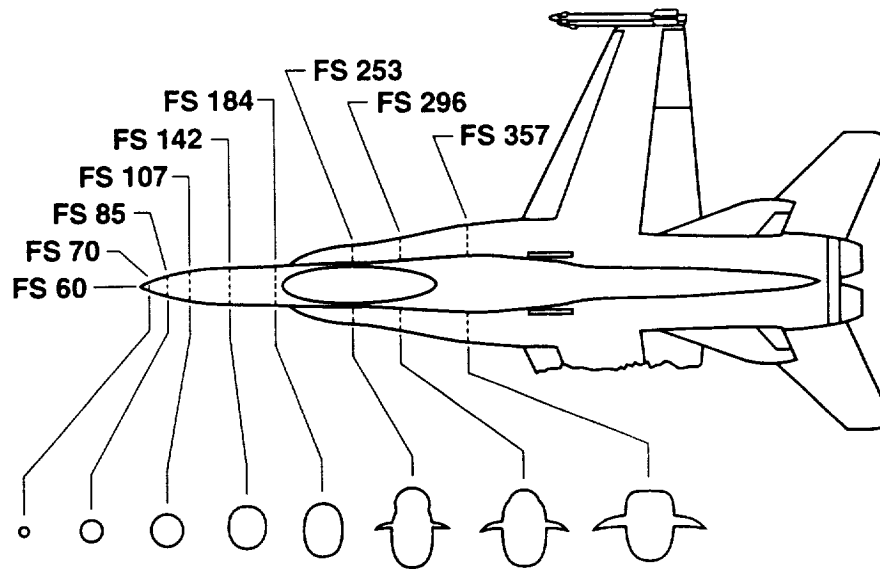


Figure 13.--Forebody and LEX surface static pressure measurement stations.

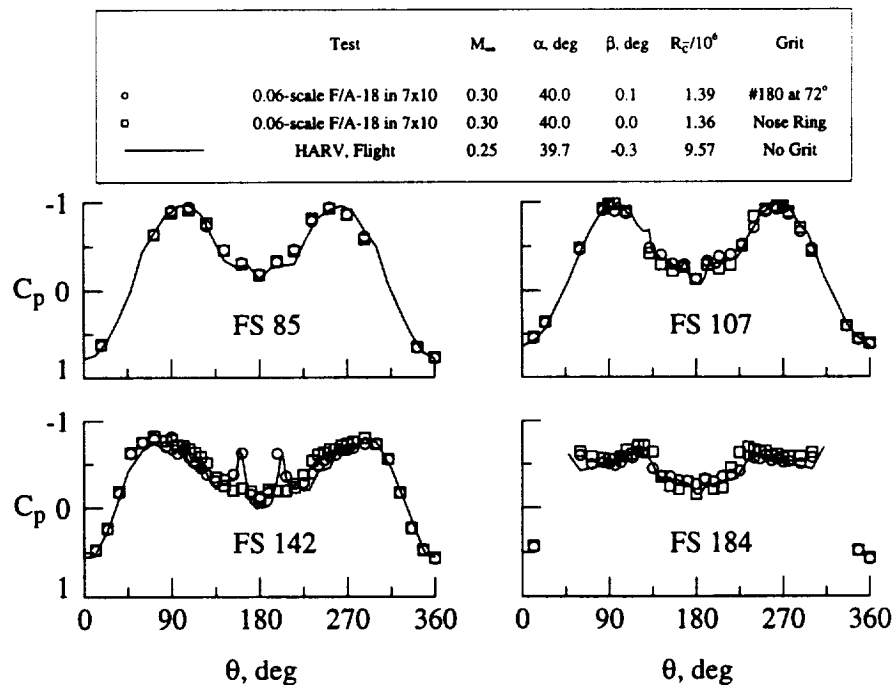


Figure 14.--Forebody pressure distributions from a 0.06-scale F/A-18 model in the 7- by 10-Foot HST with either a high- $\alpha$  gritting pattern, labeled “#180 at 72°,” or a conventional gritting pattern, labeled “Nose Ring,” compared to flight.  $\alpha = 40^\circ$ .

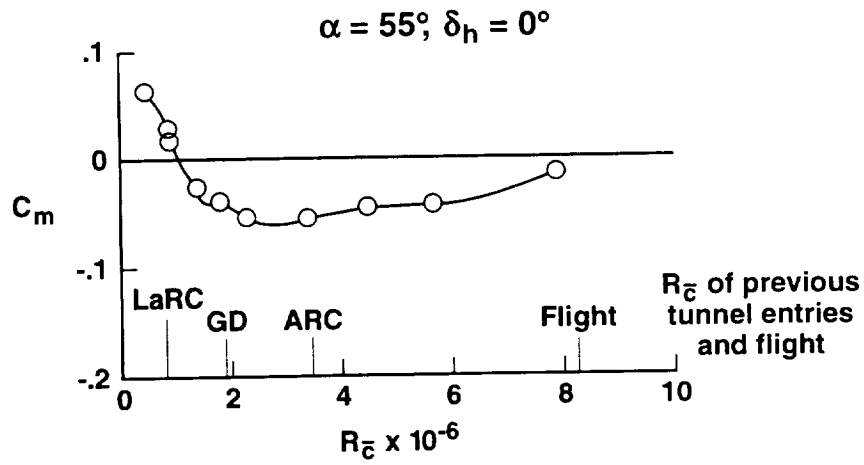


Figure 15.--Ames 12-Foot Tunnel data showing effect of  $R_{\bar{c}}$  on F-16 pitching moment.

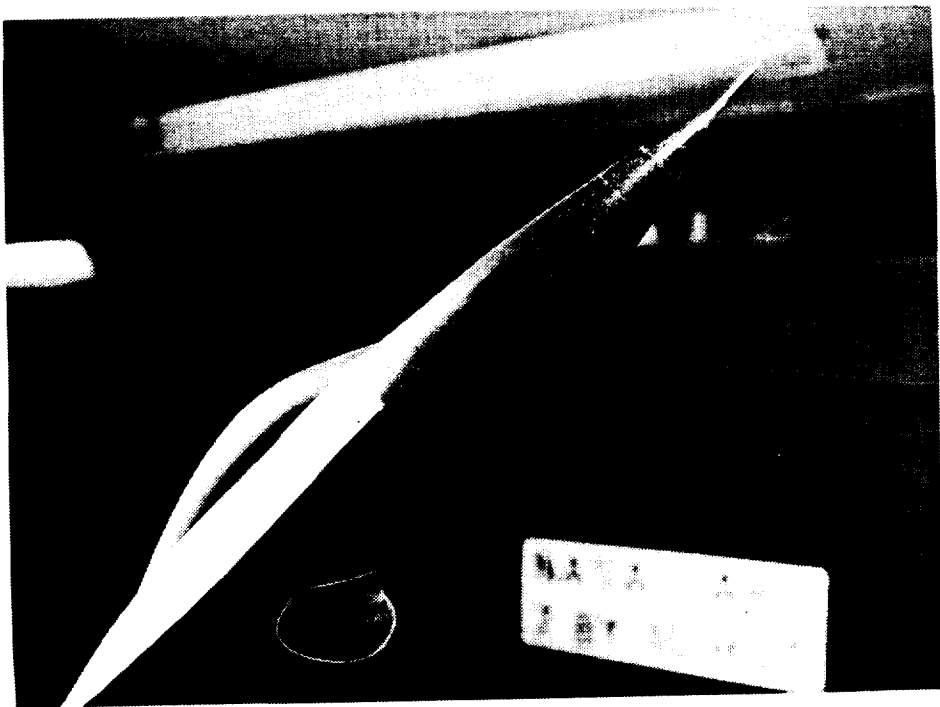


Figure 16.--Photograph of early sector grit pattern used during F-16 test in the Langley 7- by 10-Foot HST.

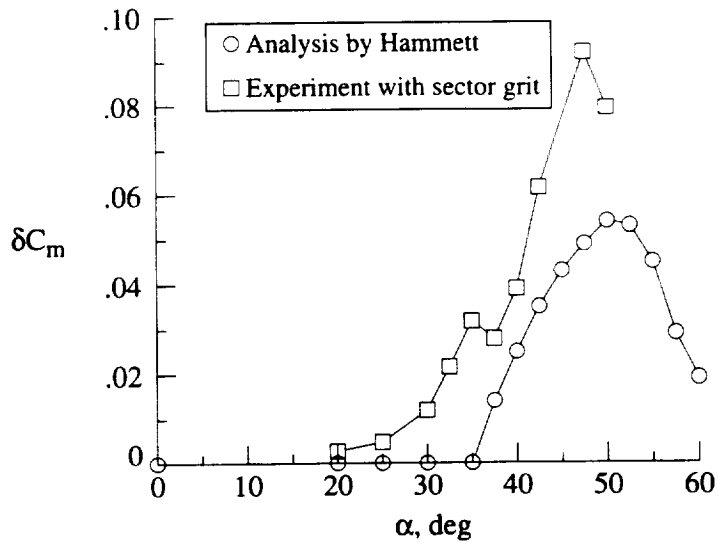


Figure 17.--Comparing predicted pitching moment increments due to  $R\bar{c}$  from post-flight test analysis by Hammett<sup>2</sup> and 7- by 10-Foot HST data with sector grit pattern.

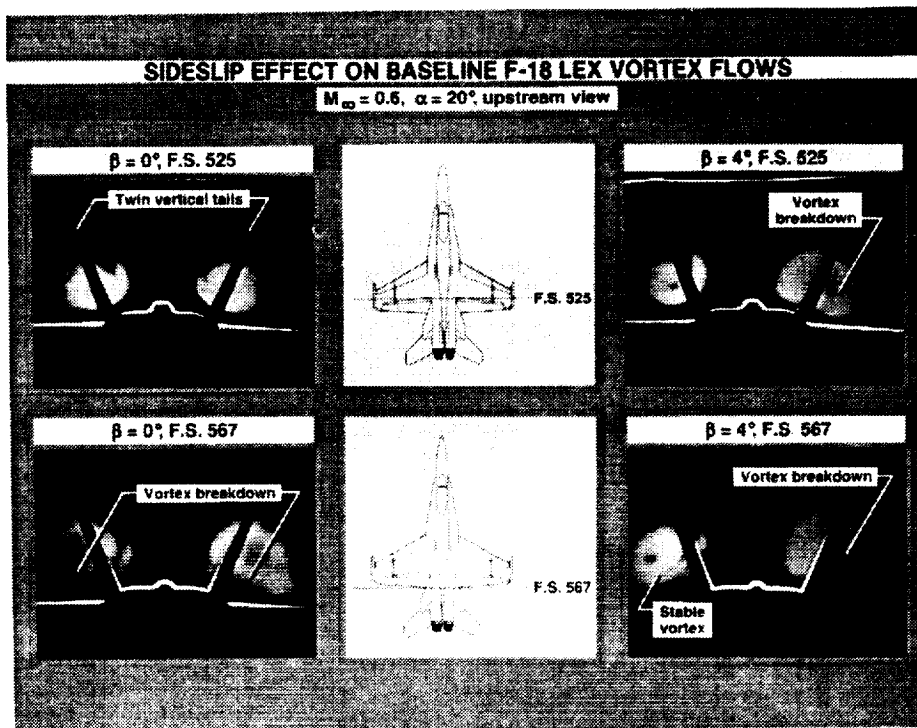


Figure 18.--Behavior of LEX vortex burst with position and angle of sideslip. Laser vapor screen images taken with the 0.06-scale F/A-18 Model in the DTRC 7- by 10-Foot Transonic Tunnel.

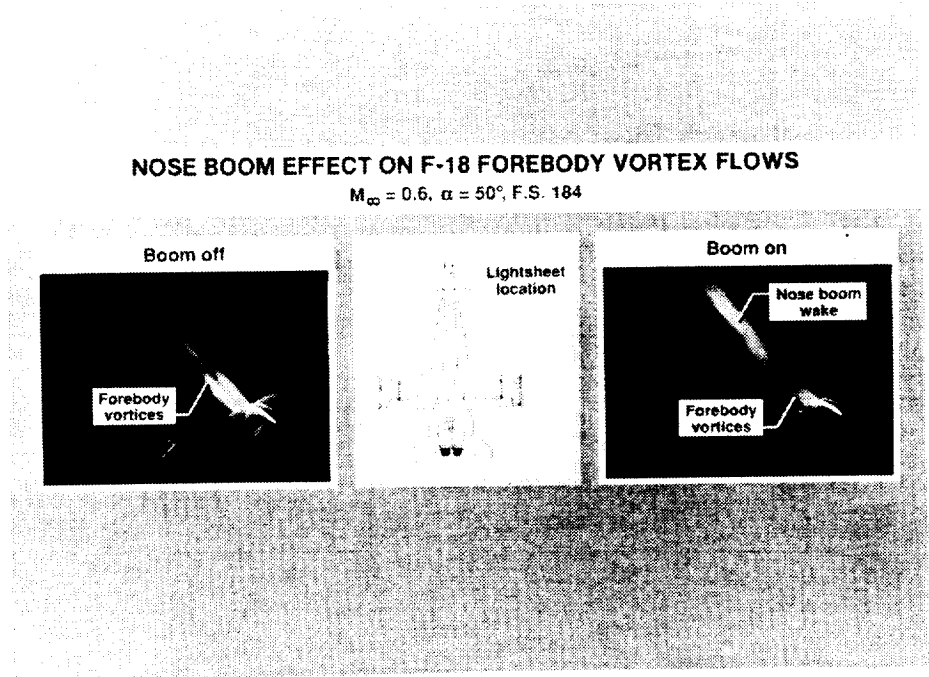


Figure 19.--Impact of NACA flight test nose boom on forebody vortices. Laser vapor screen images taken with the 0.06-scale F/A-18 Model in the DTRC 7- by 10-Foot Transonic Tunnel.

**Off-Surface Flow Visualization**

Forebody Vortex Core,  $\alpha = 25.3^\circ$ ,  $\beta = -0.5^\circ$

NASA  
A119-851

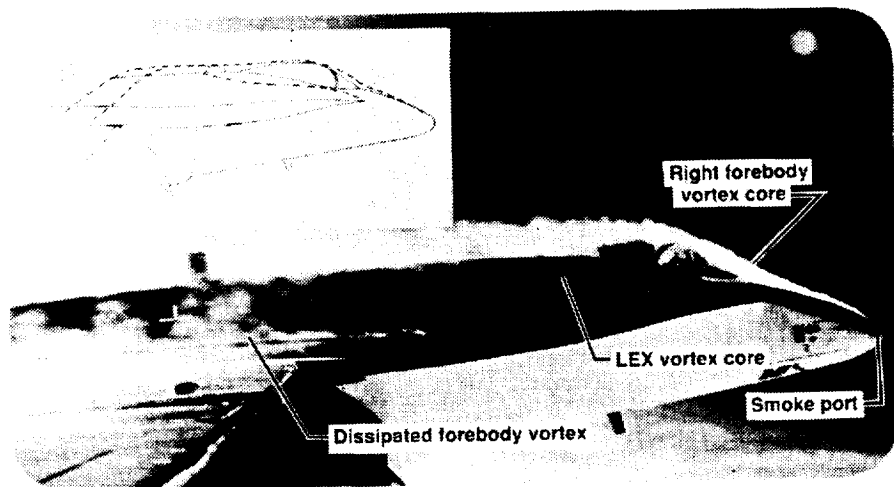


Figure 20.--Interaction between forebody and LEX vortices as visualized on the HARV vehicle.

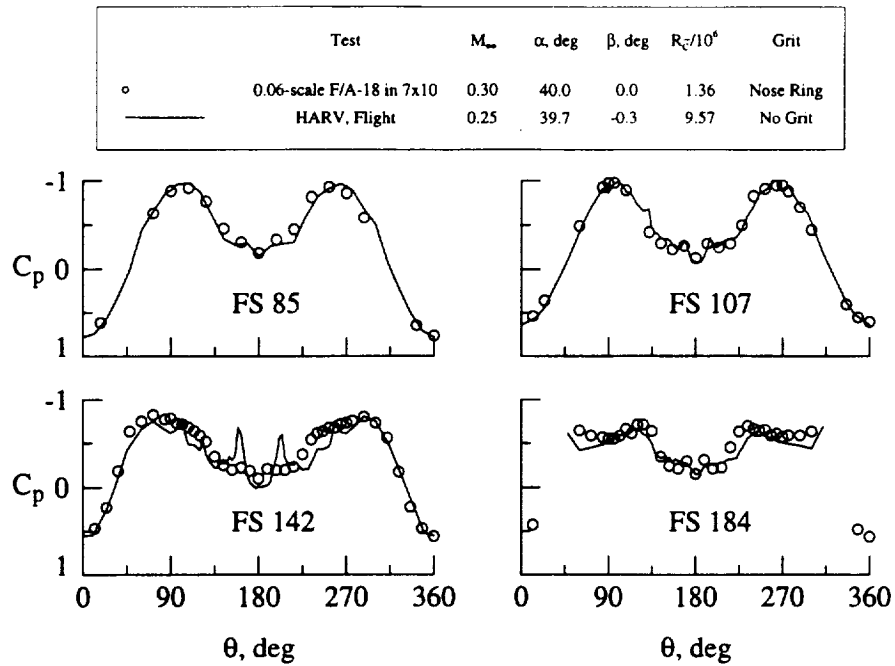


Figure 21.--Impact of  $R_{\bar{c}}$  on forebody pressures. Data from 0.06-scale F/A-18 model in the Langley 7- by 10-Foot HST compared to data from HARV vehicle.  $\alpha = 40^\circ$ .

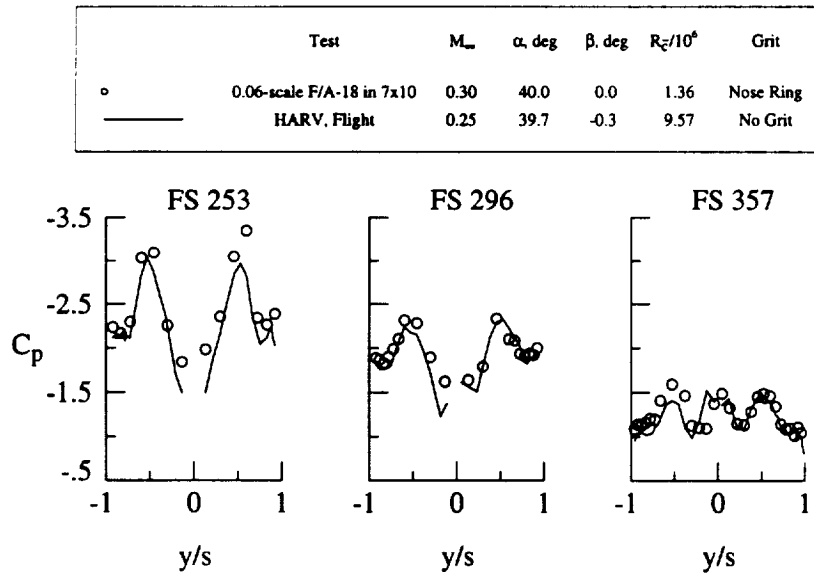


Figure 22.--Impact of  $R_{\bar{c}}$  on LEX pressures. Data from 0.06-scale F/A-18 model in the Langley 7- by 10-Foot HST compared to data from HARV vehicle.  $\alpha = 40^\circ$ .

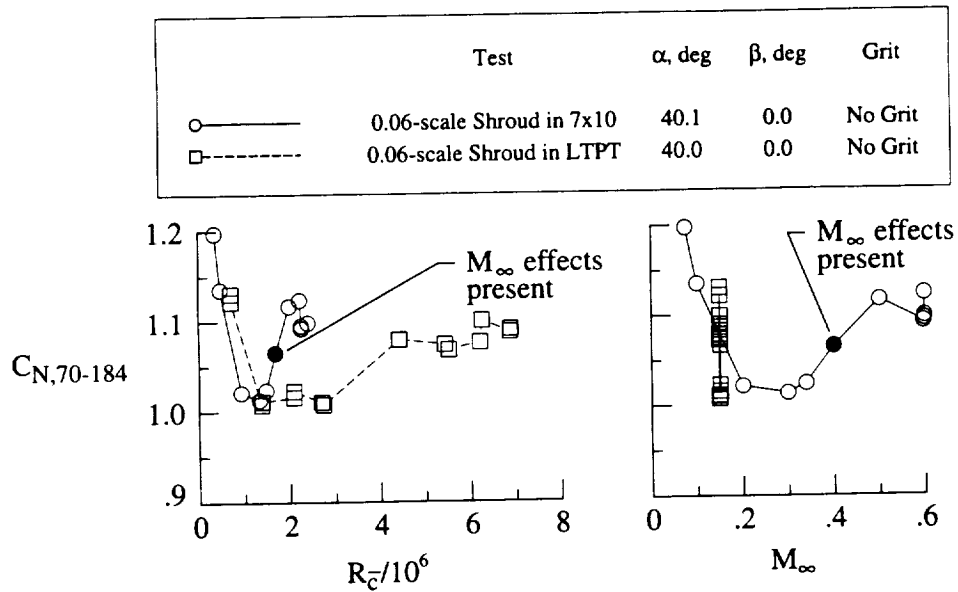


Figure 23.--Impact of  $M_{\infty}$ ,  $R_{\bar{c}}$  on normal force coefficient as integrated with pressure data for 0.06-scale Shroud model in both 7- by 10-Foot HST and in the Langley LTPT.  $\alpha = 40^\circ$ .

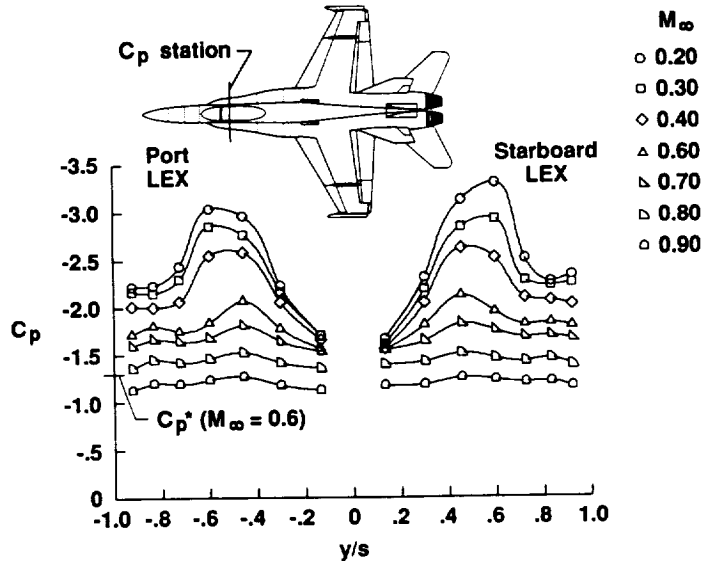


Figure 24.--Effect of  $M_{\infty}$  on LEX pressures at FS 253 for the 0.06-scale F/A-18 model in the DTRC 7- by 10-Foot Transonic Tunnel.  $\alpha = 40^\circ$ .

### MACH NUMBER EFFECT ON BASELINE F-18 LEX VORTEX FLOWS

$\alpha = 20^\circ$  F.S. 525. upstream view

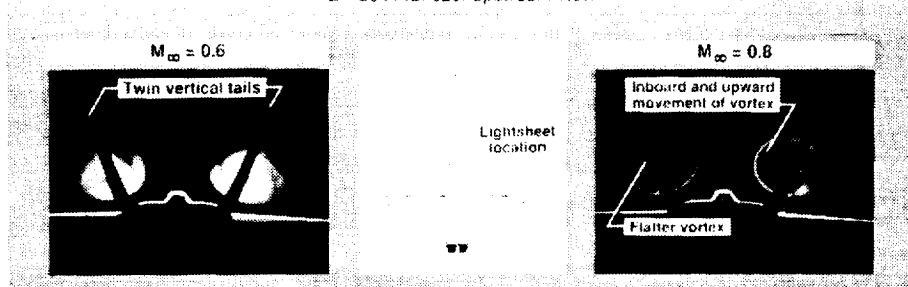


Figure 25.-- Impact of  $M_\infty$  on structure of LEX vortices as determined with the 0.06-scale F/A-18 Model in the DTRC 7- by 10-Foot Transonic Tunnel.

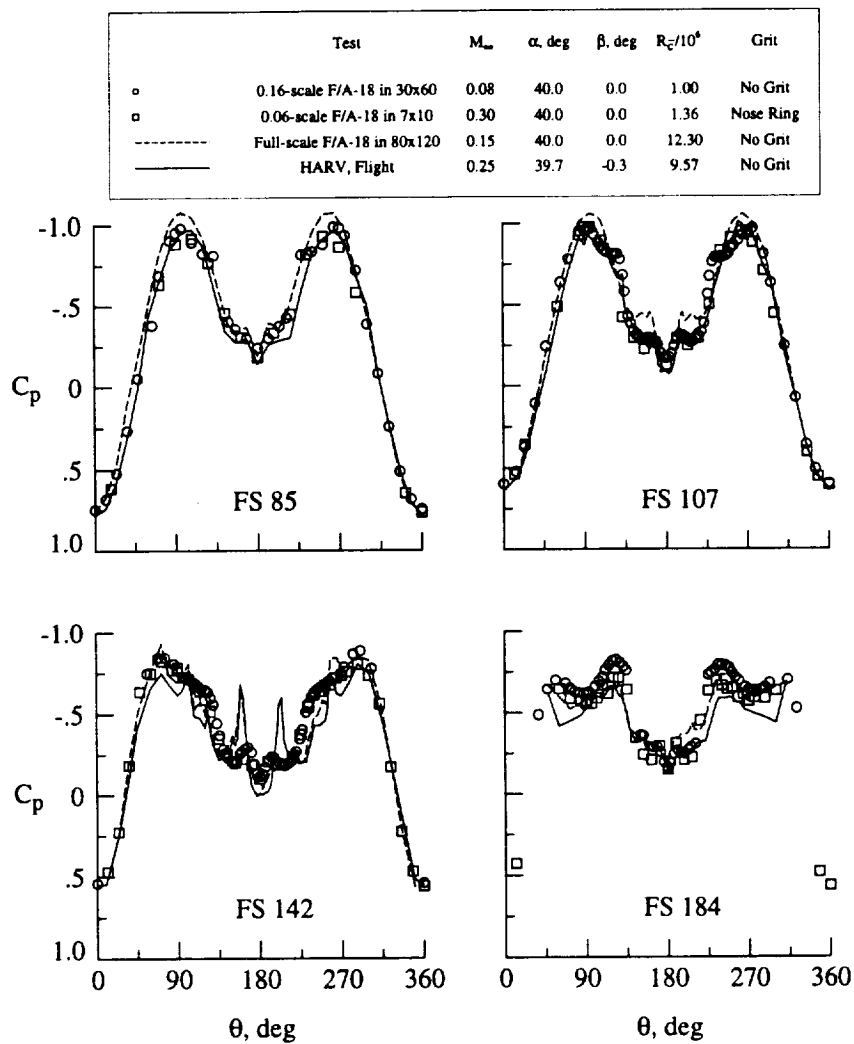


Figure 26.-- Wind tunnel forebody pressure data with conventional gritting compared to data from flight.  $\alpha = 40^\circ$ .

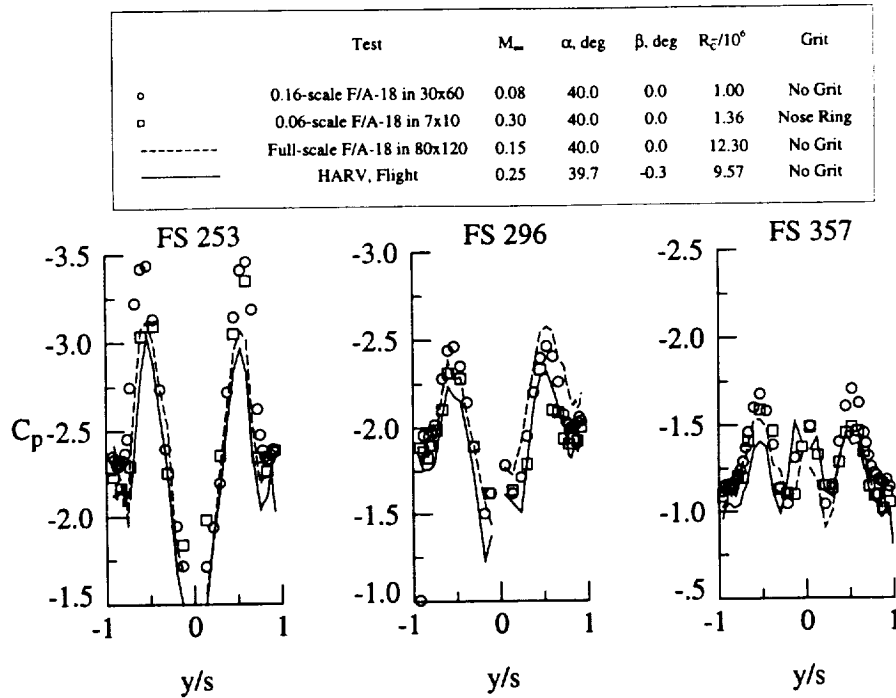


Figure 27.--Wind tunnel LEX pressure data compared to data from flight.  $\alpha = 40^\circ$ .

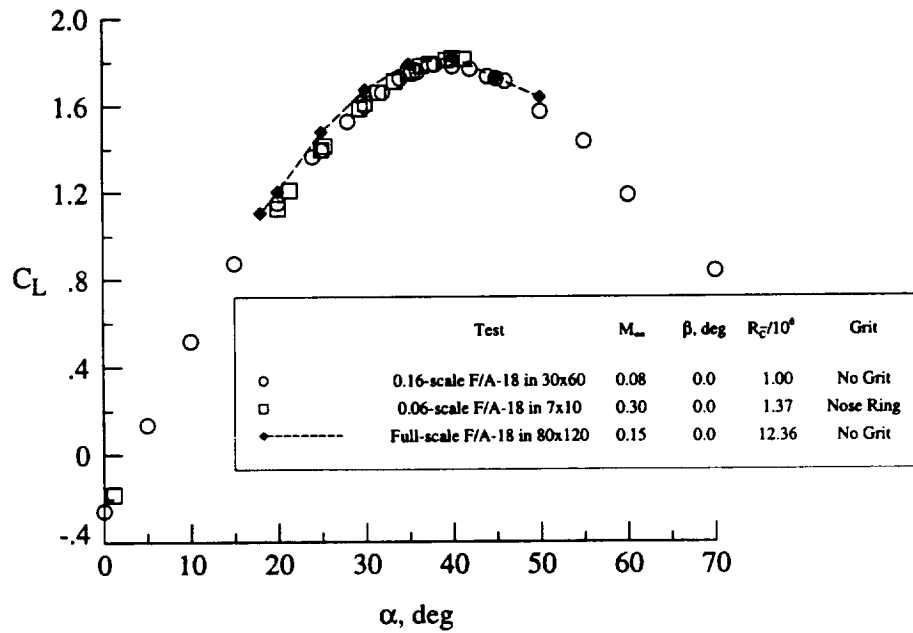


Figure 28.--Wind tunnel values of  $C_L$  compared.

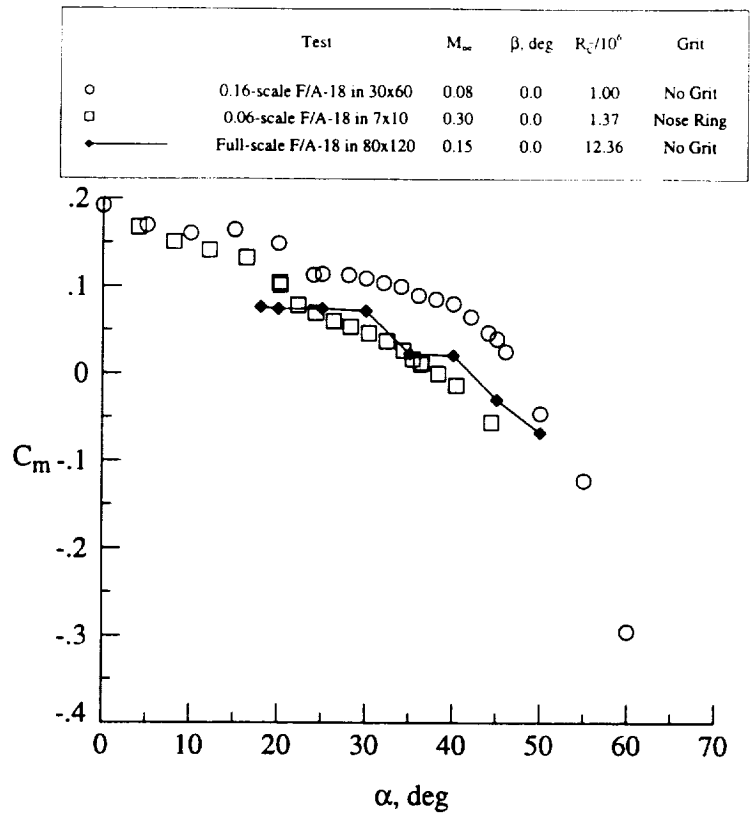


Figure 29.--Wind tunnel values of  $C_m$  compared.

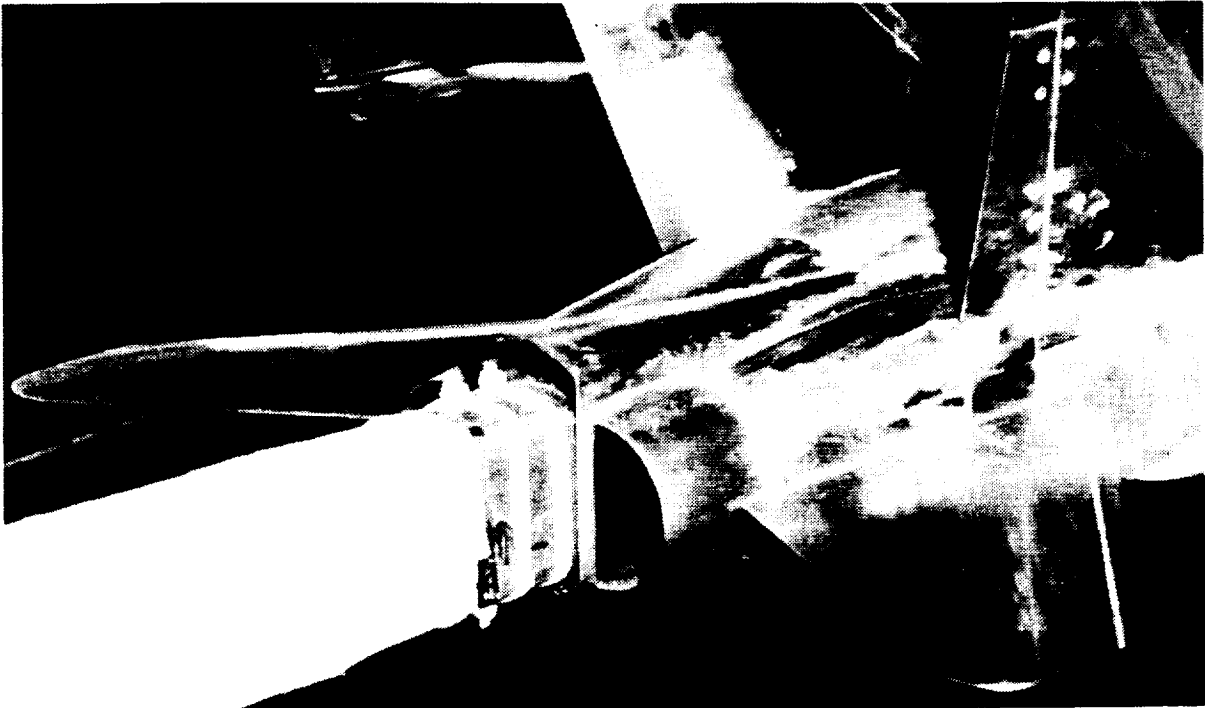
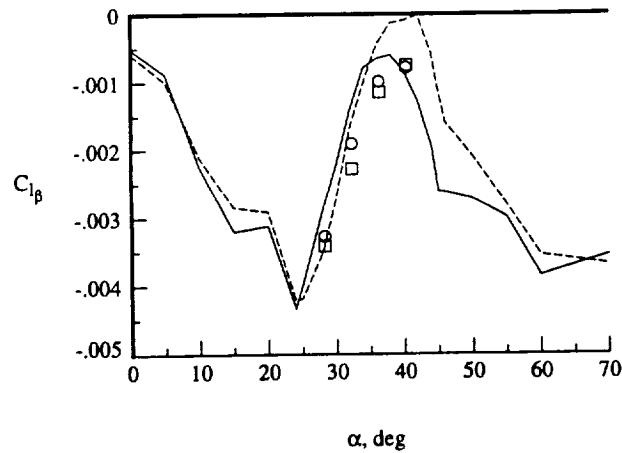


Figure 30.--Photograph showing aft end distortion for 0.06-scale model with centerline sting.

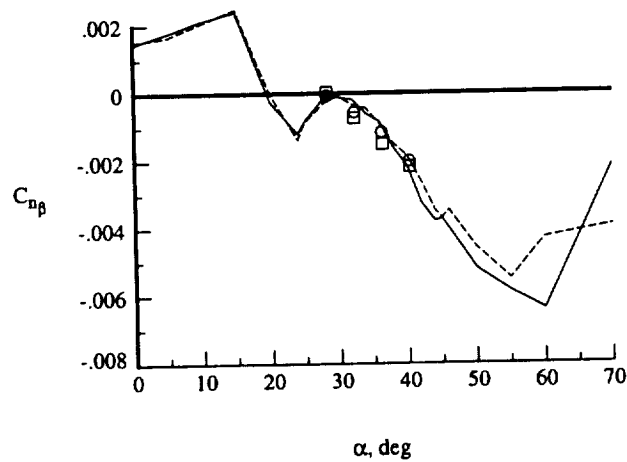
	Test	$M_\infty$	$\beta_1$ , deg	$\beta_2$ , deg	$R_z/10^4$	Grit	Forebody
○	0.06-scale F/A-18 in 7x10	0.301	-4.0	4.0	1.37	Nose Ring	Pressures
□	0.06-scale F/A-18 in 7x10	0.303	-4.0	4.0	1.45	Nose Ring	McAir
—	0.16-scale F/A-18 in 30x60	0.082	4.0	-4.0	1.00	No Grit	Pressures
- - -	0.16-scale F/A-18 in 30x60	0.082	4.0	-4.0	1.00	No Grit	No pressures



(a)  $C_{l_p}$

Figure 31.--Differences in  $C_{l_p}$  and  $C_{n_p}$  due to changes in forebody for 0.06-scale and 0.16-scale F/A-18 models.

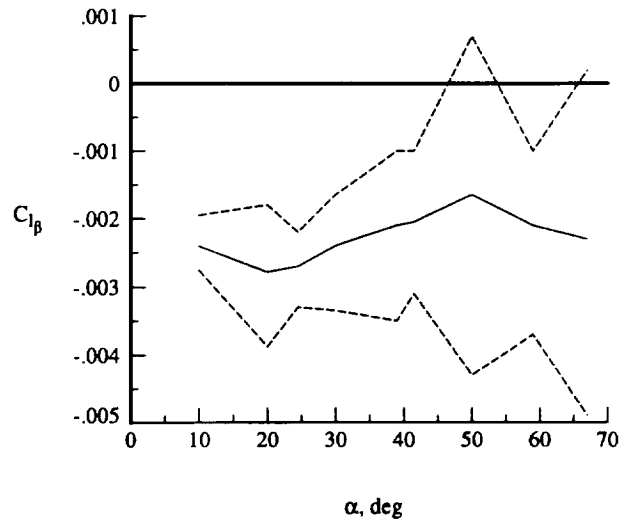
	Test	$M_\infty$	$\beta_1$ , deg	$\beta_2$ , deg	$R_z/10^4$	Grit	Forebody
○	0.06-scale F/A-18 in 7x10	0.301	-4.0	4.0	1.37	Nose Ring	Pressures
□	0.06-scale F/A-18 in 7x10	0.303	-4.0	4.0	1.45	Nose Ring	McAir
—	0.16-scale F/A-18 in 30x60	0.082	4.0	-4.0	1.00	No Grit	Pressures
- - -	0.16-scale F/A-18 in 30x60	0.082	4.0	-4.0	1.00	No Grit	No pressures



(b)  $C_{n_p}$

Figure 31.--Concluded.

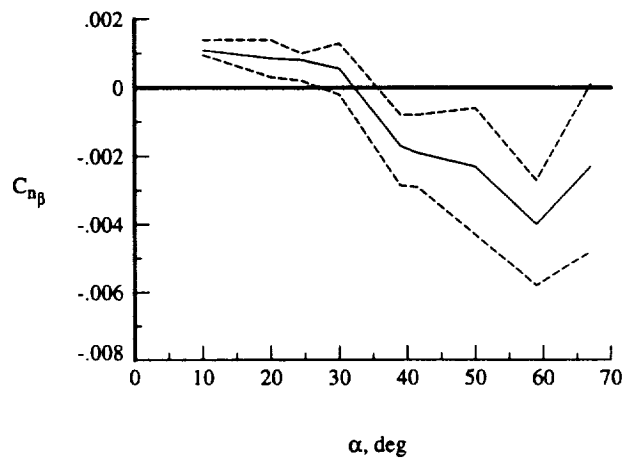
Test	M <sub>∞</sub>	β <sub>1</sub> , deg	β <sub>2</sub> , deg	R <sub>E</sub> /10 <sup>4</sup>	Grit	Forebody
HARV.Bowers	n.a.	n.a.	n.a.	n.a.	No Grit	Pressures



(a)  $C_{l\beta}$

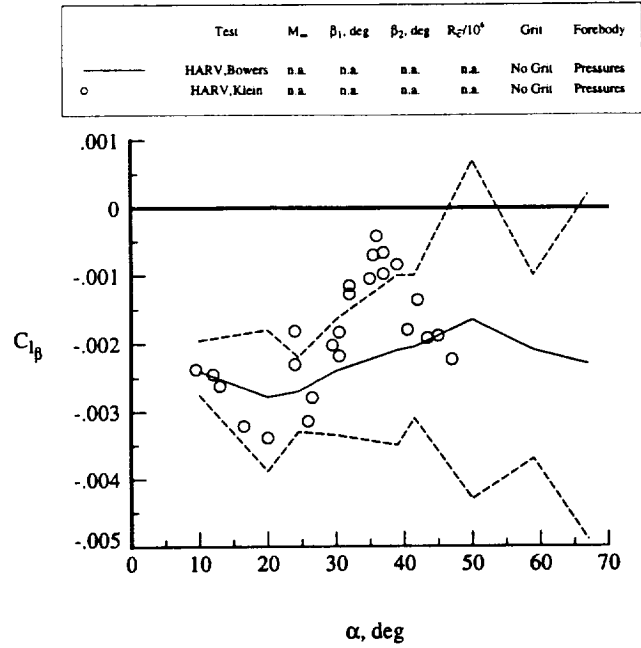
Figure 32.--HARV flight data from Bowers.

Test	M <sub>∞</sub>	β <sub>1</sub> , deg	β <sub>2</sub> , deg	R <sub>E</sub> /10 <sup>4</sup>	Grit	Forebody
HARV.Bowers	n.a.	n.a.	n.a.	n.a.	No Grit	Pressures



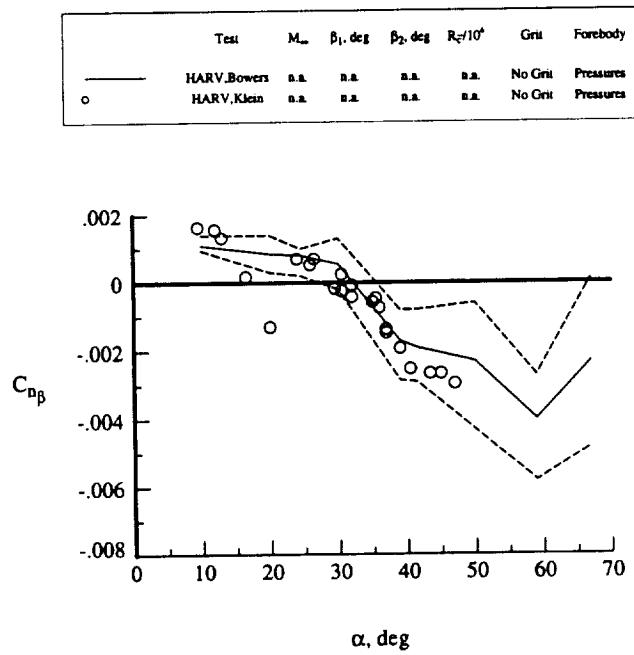
(b)  $C_{np}$

Figure 32.--Concluded.



(a)  $C_{L\beta}$

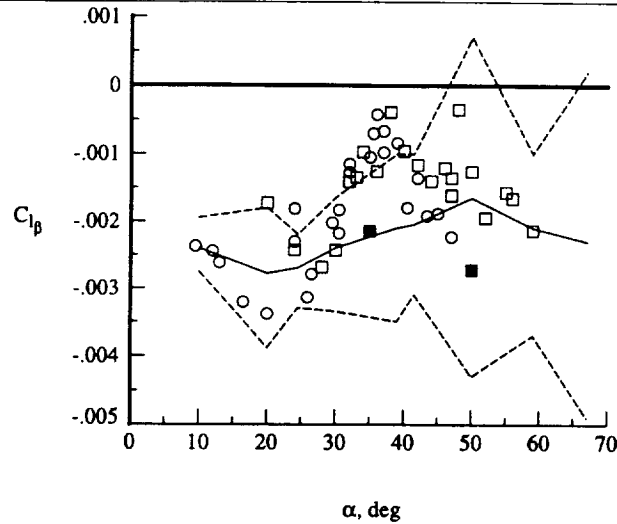
Figure 33.--HARV flight data by Klein<sup>25</sup> added to those of Bowers.



(b)  $C_{n\beta}$

Figure 33.--Concluded.

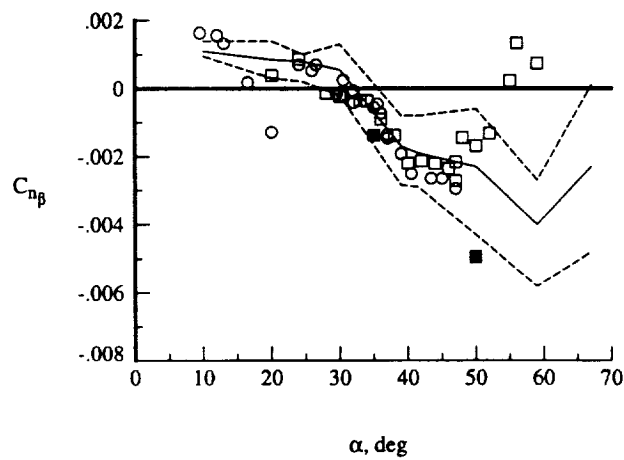
	Test	$M_\infty$	$\beta_1$ , deg	$\beta_2$ , deg	$R_z/10^4$	Grit	Forebody
—	HARV,Bowers	n.a.	n.a.	n.a.	n.a.	No Grit	Pressures
○	HARV,Klein	n.a.	n.a.	n.a.	n.a.	No Grit	Pressures
□	Full-scale F/A-18 in 80x120	0.150	4.0	-4.0	12.73	No Grit	Baseline Radome
■	Full-scale F/A-18 in 80x120	0.123	5.0	-5.0	11.09	No Grit	Strake Radome



(a)  $C_{1p}$

Figure 34.--80- by 120-Foot Wind Tunnel full-scale data added to flight data.

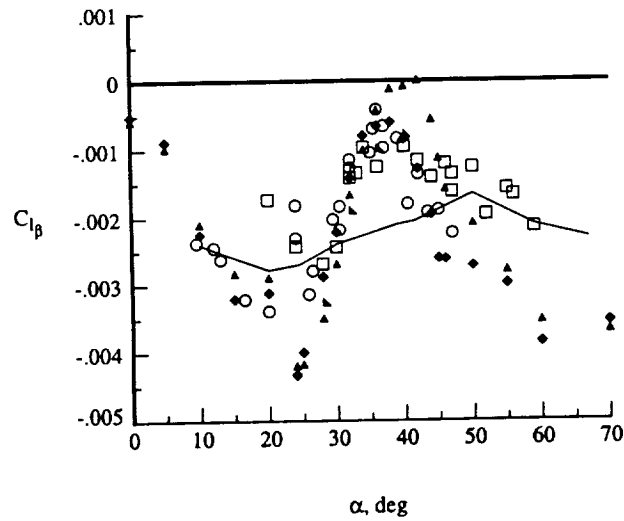
	Test	$M_\infty$	$\beta_1$ , deg	$\beta_2$ , deg	$R_z/10^4$	Grit	Forebody
—	HARV,Bowers	n.a.	n.a.	n.a.	n.a.	No Grit	Pressures
○	HARV,Klein	n.a.	n.a.	n.a.	n.a.	No Grit	Pressures
□	Full-scale F/A-18 in 80x120	0.150	4.0	-4.0	12.73	No Grit	Baseline Radome
■	Full-scale F/A-18 in 80x120	0.123	5.0	-5.0	11.09	No Grit	Strake Radome



(b)  $C_{np}$

Figure 34.--Concluded.

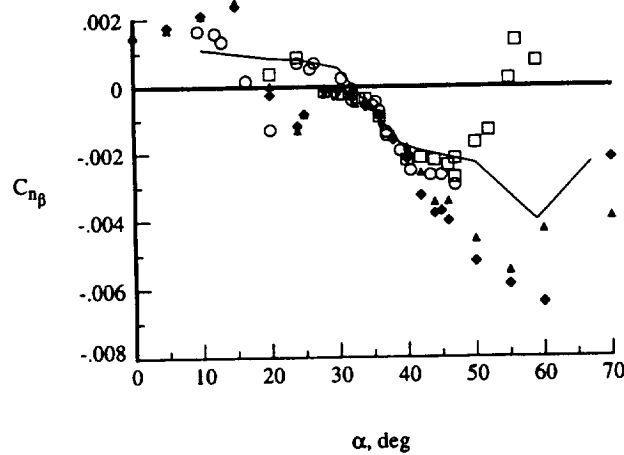
	Test	M <sub>∞</sub>	β <sub>1</sub> , deg	β <sub>2</sub> , deg	R <sub>T</sub> /10 <sup>4</sup>	Grit	Forebody
—	HARV,Bowers	n.a.	n.a.	n.a.	n.a.	No Grit	Pressures
○	HARV,Klein	n.a.	n.a.	n.a.	n.a.	No Grit	Pressures
□	Full-scale F/A-18 in 80x120	0.150	4.0	-4.0	12.73	No Grit	Baseline Radome
◆	0.16-scale F/A-18 in 30x60	0.082	4.0	-4.0	1.00	No Grit	Pressures
▲	0.16-scale F/A-18 in 30x60	0.082	4.0	-4.0	1.00	No Grit	No pressures
▲	0.06-scale F/A-18 in 7x10	0.301	-4.0	4.0	1.37	Nose Ring	Pressures



(a)  $C_{lp}$

Figure 35.--Subscale data added to that of full-scale vehicle and flight. The subscale data are for conventionally gritted models or models without any gritting.

	Test	M <sub>∞</sub>	β <sub>1</sub> , deg	β <sub>2</sub> , deg	R <sub>T</sub> /10 <sup>4</sup>	Grit	Forebody
—	HARV,Bowers	n.a.	n.a.	n.a.	n.a.	No Grit	Pressures
○	HARV,Klein	n.a.	n.a.	n.a.	n.a.	No Grit	Pressures
□	Full-scale F/A-18 in 80x120	0.150	4.0	-4.0	12.73	No Grit	Baseline Radome
◆	0.16-scale F/A-18 in 30x60	0.082	4.0	-4.0	1.00	No Grit	Pressures
▲	0.16-scale F/A-18 in 30x60	0.082	4.0	-4.0	1.00	No Grit	No pressures
▲	0.06-scale F/A-18 in 7x10	0.301	-4.0	4.0	1.37	Nose Ring	Pressures



(b)  $C_{np}$

Figure 35.--Concluded.

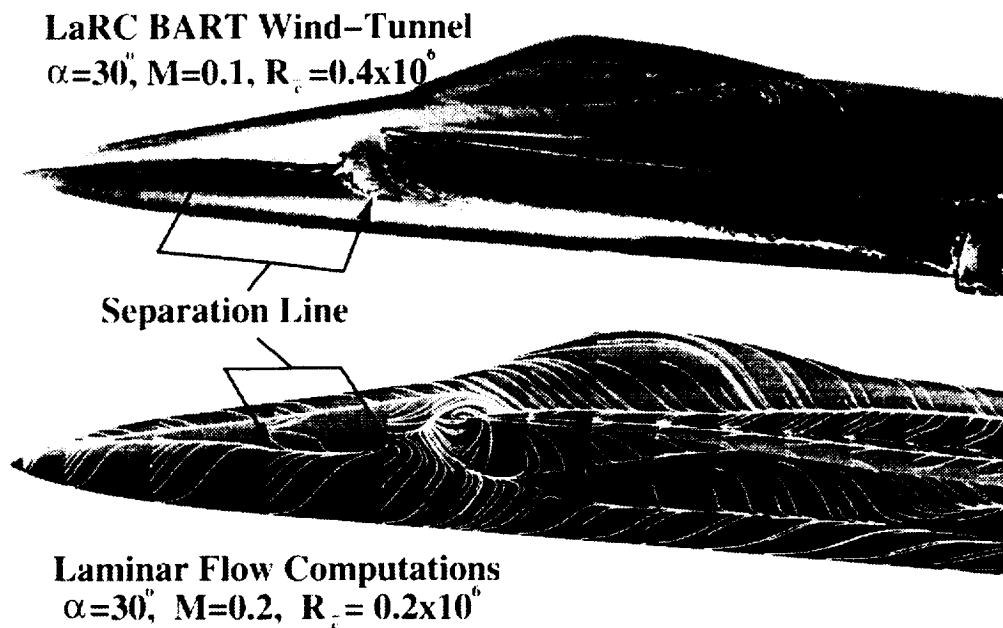


Figure 36.--Early Navier-Stokes predictions of surface flow patterns compared to test in Langley BART tunnel designed to insure laminar flow.

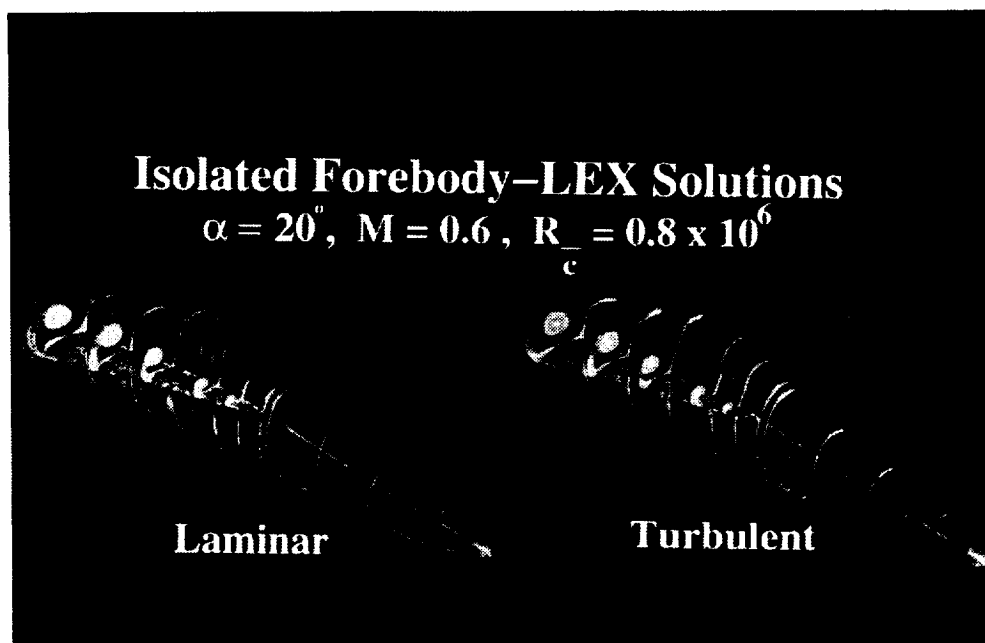


Figure 37.--Early CFD solutions on configuration consisting of F/A-18 forebody, LEX's, and constant cross section downstream extension.

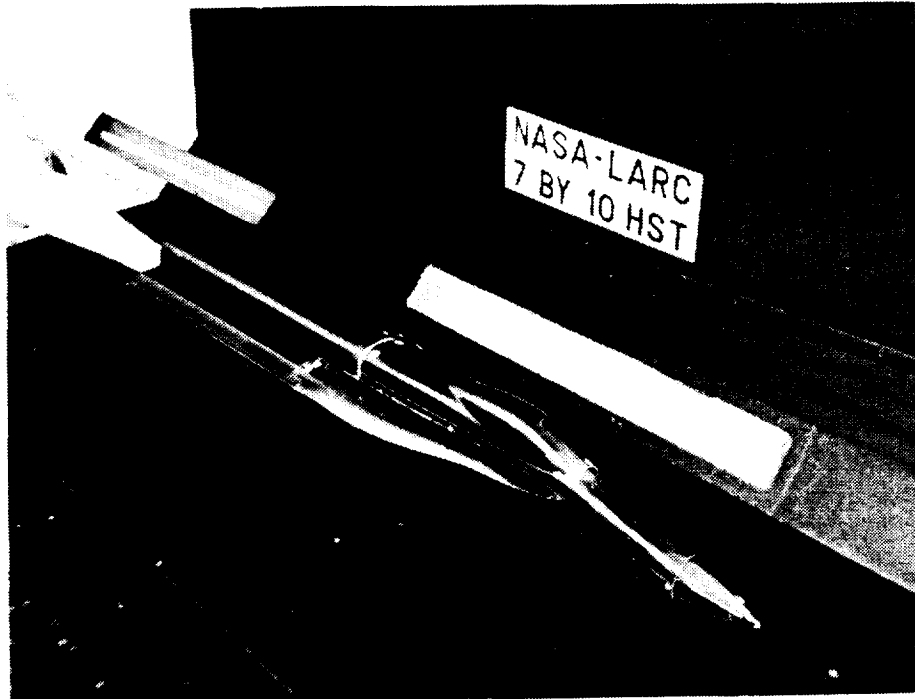


Figure 38.--0.06-scale Shroud model designed to match early CFD configuration. Shown in Langley 7- by 10-Foot HST.

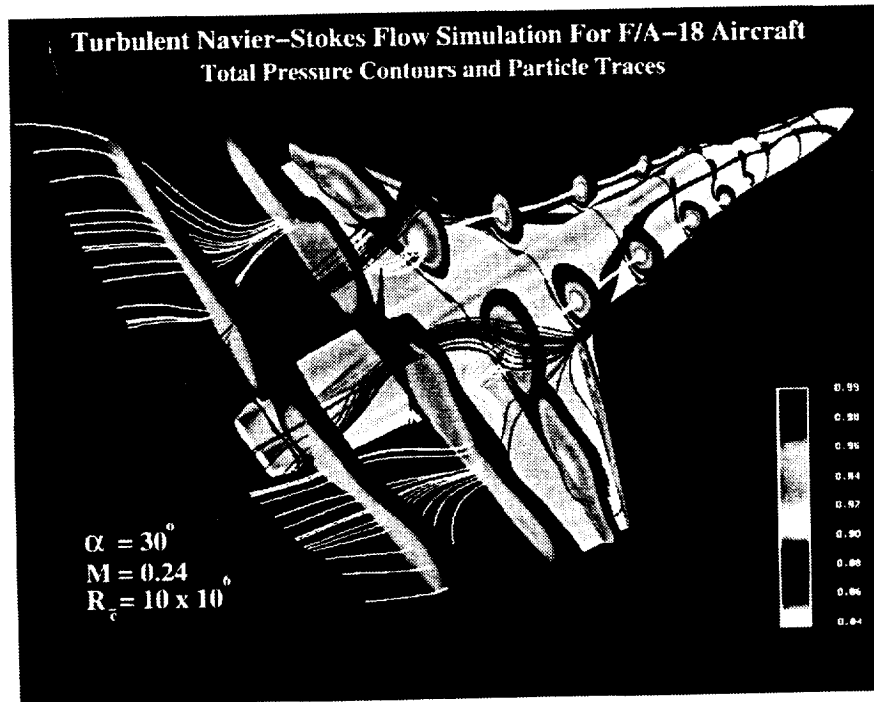


Figure 39.--CFD solution over modified F/A-18 configuration that did not include vertical tails, horizontal tails, or flow-through inlets.

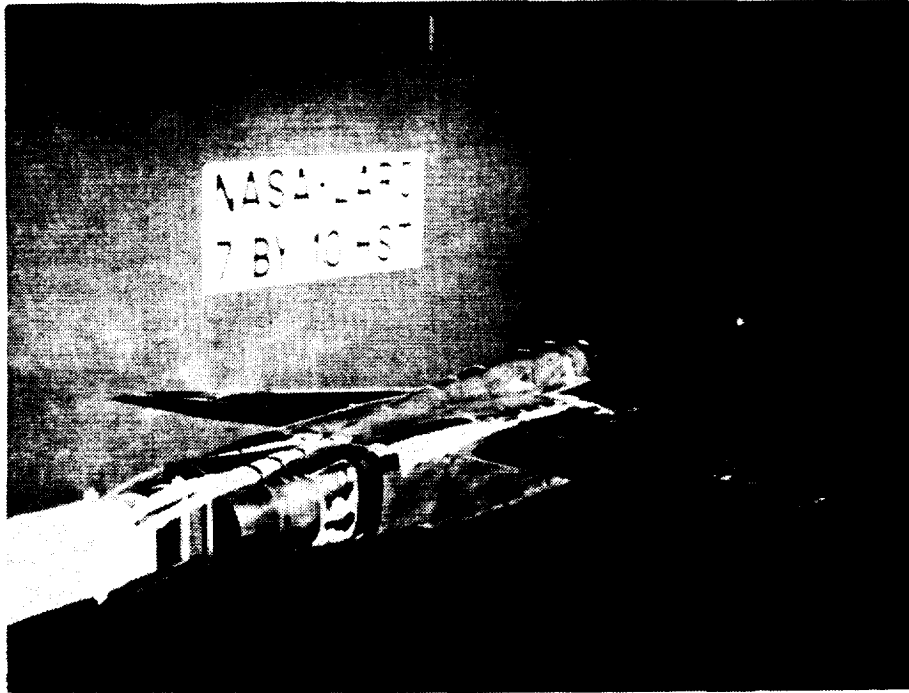


Figure 40.--Modified 0.06-scale model F/A-18 configuration simulating CFD configuration without vertical tails, horizontal tails, or flow-through inlets.